Source details

Nuclear Engineering and Design

See also: Nuclear Engineering and Design/Fusion

Scopus coverage years: from 1965 to Present

Publisher: Elsevier

ISSN: 0029-5493

Subject area: Energy: Nuclear Energy and Engineering | Engineering: Safety, Risk, Reliability and Quality | Physics and Astronomy: Nuclear and High Energy Physics | Engineering: Mechanical Engineering | View all

Source type: Journal

CiteScore 2022
3.4

SJR 2022
0.853

SNIP 2022
1.234

View all documents > | Set document alert | Save to source list | Source Homepage

CiteScore | CiteScore rank & trend | Scopus content coverage

i Improved CiteScore methodology

CiteScore 2022 counts the citations received in 2019-2022 to articles, reviews, conference papers, book chapters and data papers published in 2019-2022, and divides this by the number of publications published in 2019-2022. Learn more >

CiteScore 2022

$$3.4 = \frac{\text{5,931 Citations 2019 - 2022}}{\text{1,734 Documents 2019 - 2022}}$$

Calculated on 05 May, 2023

CiteScoreTracker 2023

$$3.0 = \frac{\text{5,005 Citations to date}}{\text{1,660 Documents to date}}$$

Last updated on 05 August, 2023 • Updated monthly

CiteScore rank 2022

Category	Rank	Percentile
Energy — Nuclear Energy and Engineering	#27/68	61st
Engineering — Safety, Risk, Reliability and Quality	#76/192	60th

View CiteScore methodology > | CiteScore FAQ > | Add CiteScore to your site

Nuclear Engineering and Design

COUNTRY

Netherlands

Universities and research institutions in Netherlands

Media Ranking in Netherlands

SUBJECT AREA AND CATEGORY

Energy
- Nuclear Energy and Engineering

Engineering
- Mechanical Engineering
- Safety, Risk, Reliability and Quality

Environmental Science
- Waste Management and Disposal

Materials Science
- Materials Science (miscellaneous)

Physics and Astronomy
- Nuclear and High Energy Physics

PUBLISHER

Elsevier BV

H-INDEX

115

PUBLICATION TYPE

Journals

ISSN

00295493

COVERAGE

1965-2022

INFORMATION

Homepage

How to publish in this journal

Contact

SCOPE

Nuclear Engineering and Design covers the wide range of disciplines involved in the engineering, design, safety and construction of nuclear fission reactors. The Editors welcome papers both on applied and innovative aspects and developments in nuclear science and technology. Fundamentals of Reactor Design include: • Thermal-Hydraulics and Core Physics • Safety Analysis, Risk Assessment (PSA) • Structural and Mechanical Engineering • Materials Science • Fuel Behavior and Design • Structural Plant Design • Engineering of Reactor Components • Experiments Aspects beyond fundamentals of Reactor Design covered: • Accident Mitigation Measures • Reactor Control Systems • Licensing Issues • Safeguard Engineering • Economy of Plants • Reprocessing / Waste Disposal • Applications of Nuclear Energy • Maintenance • Decommissioning Papers on new reactor ideas and developments (Generation IV reactors) such as inherently safe modular HTRs, High Performance LWRs/HWRs and LMFBs/GFR will be considered; Actinide Burners, Accelerator Driven Systems, Energy Amplifiers and other special designs of power and research reactors and their applications are also encouraged.

Join the conversation about this journal

Quartiles

FIND SIMILAR JOURNALS

1
Hedongli Gongcheng/Nuclear Power Engineering
CHN
87%
similarity

2
Science and Technology of Nuclear Installations
EGY
85%
similarity

3
Journal of Nuclear Engineering and Radiation
USA
72%
similarity

4
Annals of Nuclear Energy
GBR
65%
similarity

5
Pro
GBR

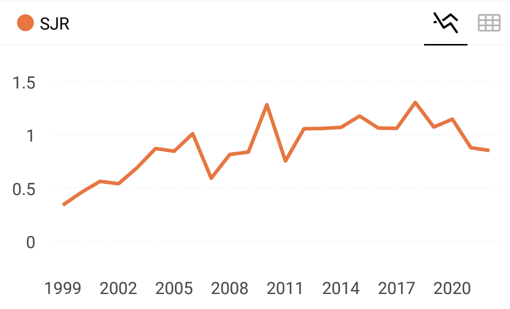

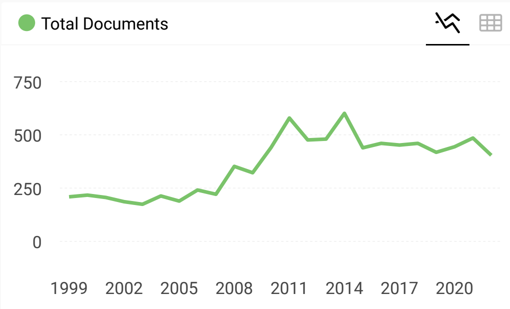

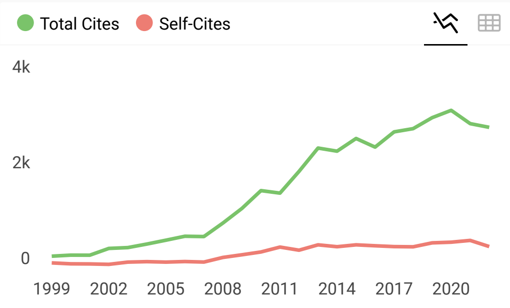

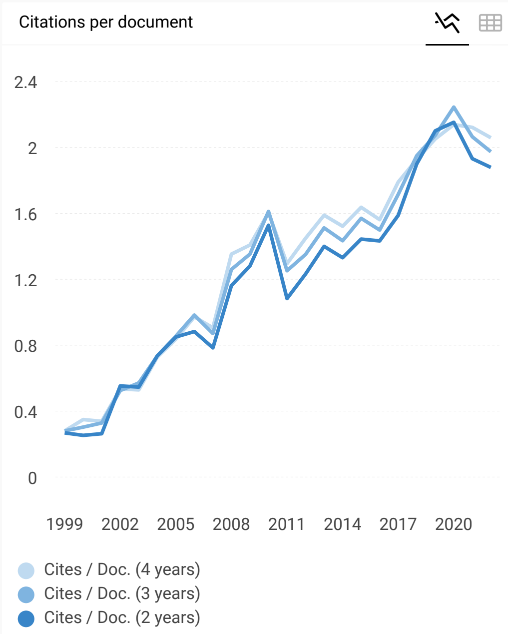

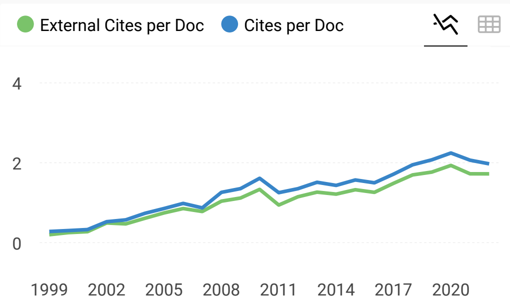

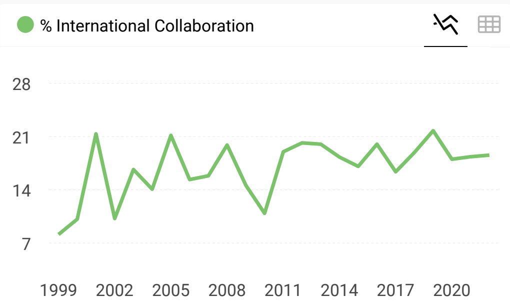

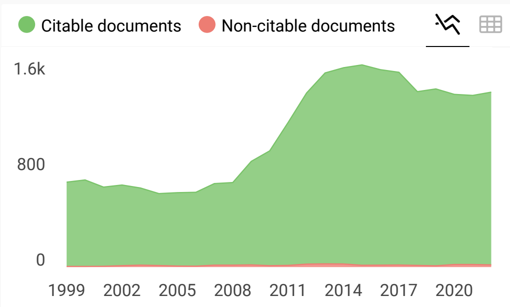

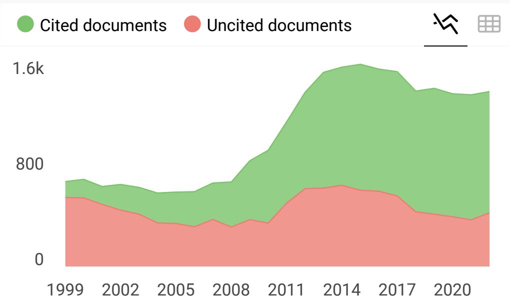

← Show this widget in your own website

Just copy the code below and paste within your html code:

<a href="https://www.scimag

VOLUME 412 OCTOBER 2023 ISSN 0029-5493

Nuclear Engineering and Design

An International Journal devoted to all aspects of Nuclear Fission Energy

Available online at www.sciencedirect.com

ScienceDirect

Affiliated with the European Nuclear Society (ENS) and with the International Association for Structural Mechanics in Reactor Technology, e.V. (IASMiRT)

NUCLEAR ENGINEERING AND DESIGN

Abstracted/Indexed in: *Applied Mechanical Reviews, Cambridge Scientific Abstracts, Chemical Abstract, Current Contents, Ei Compendex Plus, Ei Engineering, Energy Science and Technology, Fuel and Energy Abstracts, INSPEC, SciScearch, METADEX, PASCAL/CNRS.* Also covered in the abstract and citation database SCOPUS®. Full text available on ScienceDirect®.

Volume 404

1 April 2023

Download full issue

Previous vol/issue

Next vol/issue

A.I. Popescu, D.H. Barber, T. Daniels, H. Albasha, ... R. Murphy-Snow
Article 112187

Article preview

Core Physics

Research article ○ Abstract only

The low-enriched uranium core design of a MW heat pipe cooled reactor

Yunqin Wu, Youqi Zheng, Yushan Tao, Xiaoyue Liu, ... Yongping Wang
Article 112195

Article preview

Thermal Hydraulics

Research article ○ Abstract only

LES simulation on heavy liquid metal flow in a bare rod bundle for assessment of turbulent Prandtl number

Yiqi Yu, Emily Shemon, Elia Merzari
Article 112175

Article preview

Research article ○ Abstract only

Large-eddy simulation on two-liquid mixing in the horizontal leg and downcomer (the TAMU-CFD Benchmark), with respect to fluctuation behavior of liquid concentration

Satoshi Abe, Yuria Okagaki
Article 112165

Article preview

Research article ○ Abstract only

An integrated coupling model for solving multiscale fluid-fluid coupling problems in SAM code

Guojun Hu, Ling Zou, Daniel J. O'Grady, Rui Hu
Article 112186

Article preview

Research article ○ Abstract only

Statistical characterization of the interfacial behavior captured by a novel image processing algorithm during the gas/liquid counter-current two-phase flow in a 1/3 scaled down of PWR hot leg

Achilleus Hermawan Astyanto, Akhlisa Nadiantya Aji Nugroho, Indarto, I Gusti Ngurah Bagus Catrawedarma, ... Deendarlianto
Article 112179

Article preview

Research article ○ Abstract only

Performance analysis of heat transfer for supercritical water cooled in various inclined tubes

Shang Mao, Tao Zhou, Chunhui Xue, Dong Wei
Article 112184

Article preview

Research article ○ Abstract only

Investigation on separation characteristics of gas–liquid two-phase flow around the perforated tube

Jinzhi Wang, Yechun Wang, Xiangdong Xie, Qiang Xu, ... Liejin Guo
Article 112200

Article preview

View PDF Article preview

Research article ○ Abstract only

Attention-based time series analysis for data-driven anomaly detection in nuclear power plants

Feiyan Dong, Shi Chen, Kazuyuki Demachi, Masanori Yoshikawa, ... Shigeru Takaya
Article 112161

Article preview

Research article ○ Abstract only

Modeling and assessment of human and organization factors of nuclear safety culture in Saudi Arabia

Salman M. Alshehri, Salman M. Alzahrani, Anas M. Alwafi
Article 112176

Article preview

Research article ○ Abstract only

Effect of interfacial area modeling method on interfacial drag predictions for two-fluid model calculations in large diameter pipes

Alexander Swearingen, Joshua P. Schlegel, Takashi Hibiki
Article 112180

Article preview

Research article ○ Abstract only

Research on simplification of branches method of accident sequences based on expert knowledge and heuristic optimization algorithm

Dabin Sun, Lei Li, Zhaofei Tian, He Wang, Guangliang Chen
Article 112198

Article preview

Research article ○ Abstract only

High Temperature Test Facility sensitivity and calibration studies to inform OECD-NEA benchmark calculations

Robert F. Kile, Aaron S. Epiney, Nicholas R. Brown
Article 112178

Article preview

Research article ● *Open access*

A comparative simulation of severe accident progressions by CINEMA and MAAP5

JinHo Song, DongGun Son, JaeHyun Ham, JunHo Bae, ... YuJung Choi
Article 112181

View PDF Article preview

Research article ○ Abstract only

Insights in the safety analysis of an early microreactor design

Federico Antonello, Jacopo Buongiorno, Enrico Zio
Article 112203

Article preview

Instrumentation and Control

Research article ○ Abstract only

Batch Deterministic and Stochastic Petri nets Modeling for Reliability Quantification for Safety Critical Systems of Nuclear Power Plants

Nand Kumar Jyotish, Lalit Kumar Singh, Chiranjeev Kumar, Pooja Singh
Article 112191

Article preview

Nuclear Engineering and Design 404 (2023) 112179

Contents lists available at ScienceDirect

Nuclear Engineering and Design

journal homepage: www.elsevier.com/locate/nucengdes

Statistical characterization of the interfacial behavior captured by a novel image processing algorithm during the gas/liquid counter-current two-phase flow in a 1/3 scaled down of PWR hot leg

Achilleus Hermawan Astyanto [a,b], Akhlisa Nadiantya Aji Nugroho [c], Indarto [a,c], I Gusti Ngurah Bagus Catrawedarma [d], Dirk Lucas [e], Deendarlianto [a,c,*]

[a] Department of Mechanical and Industrial Engineering, Universitas Gadjah Mada, Jalan Grafika No 2 Kampus UGM, Yogyakarta 55281, Indonesia
[b] Department of Mechanical Engineering, Universitas Sanata Dharma, Kampus III USD Maguwoharjo, Yogyakarta 55282, Indonesia
[c] Center of Energy Studies, Universitas Gadjah Mada, Sekip K-1A Kampus UGM, Yogyakarta 55281, Indonesia
[d] Department of Mechanical Engineering, Politeknik Negeri Banyuwangi, Jalan Raya Jember km 13, Lebanasem, Banyuwangi 68461, Indonesia
[e] Helmholtz-Zentrum Dresden-Rossendorf e.V., Institute of Fluid Dynamics, Dresden 01328, Germany

A B S T R A C T

This study addresses a statistical characterization of the interfacial behaviors during gas/liquid counter-current flow in a large scale of pressurized water reactor's hot leg typical geometry on the basis of both time and frequency domain analyses. Here, the visualizations were captured by high-speed cameras. Furthermore, the image processing algorithm on the basis of pixel identification was developed to identify the time-series interfacial dynamics of the liquid holdup fluctuations, comprising the wave growth and its movement. The obtained data were further analyzed by using various advanced statistical tools comprising the probability density function, power spectral density function, and also discrete wavelet transform. Additionally, chaotic levels of the flow were obtained through the Kolmogorov-entropy analysis.

Particular results reveal that a typical mechanism of flooding begins with the appearance of a wavy interface which further develops into either a roll or large wave, and later blocks the entire cross-sectional area of the conduit around the bend region. This later stage indicates the inception of flooding which is characterized by the increase of the water level close to the bend region. Next, the higher the pressure of system, the higher the frequency occurrence of slugging, while the injected gas flow rate obtained a different trend. However, the Kolmogorov entropy enables to correlate the stabilizing effect due to the fluid resistance which corresponds to either the pressure of the system or the physical properties of the fluid. In addition, there were no significant differences between the flooding mechanisms for both the air/water and steam/water flows.

1. Introduction

In a pressurized water reactor (PWR), the steam generator (SG) transfers heat from a primary coolant (15 MPa of pressurized water) to a secondary coolant (7 MPa of pressurized water/steam) via a U-shaped pipe to produce superheated vapor. Here, the primary coolant water is heated in a reactor pressure vessel (RPV) before being pumped to the SG via a conduit called the hot leg which is comprised by a combination of a horizontal channel and a riser which is connected by an elbow. For a hypothetical loss-of-coolant accident (LOCA) or so-called mid-loop operation, such scenarios must be comprehensively considered. This corresponds to the water level in the RPV which falls below the hot leg nozzle since the steam produced in the RPV and flowing via the hot leg towards the steam generator maybe condensed. The condensate may flow back to the RPV in counter-current to the steam, establishes a natural circulation, and contributes to the reactor core cooling. However, in the hot leg, the onset of flooding, which is also called as counter-current flow limitation (CCFL), and followed by the zero liquid penetration (ZLP), may hinder this two-phase natural circulation. Once the steam mass flow rate reaches a certain value, the accumulated steam may clog the hot leg channel. It further prevents the cooling water to flow from the SG to the RPV (Deendarlianto et al., 2012b; Vallée et al., 2012b). Under a component failure situation, an emergency mitigation toward this counter-current two-phase flow (CCF) phenomenon must be well prepared to ensure that reactor core cooling can continue to operate.

Over several decades, CCF phenomena obtain specific attentions, and has been extensively investigated during the safety analysis on the operation of PWR. Numerous authors have reported both analytical and experimental investigations on the factors governing the concerning flow phenomena. They might correspond to the characteristics of the flow regimes which were approached by empirical data evaluations under various conditions (Wallis, 1961), the scaling sizes and geometries

* Corresponding author at: Department of Mechanical and Industrial Engineering, Universitas Gadjah Mada, Jl. Grafika No 2, Yogyakarta 55281, Indonesia.
E-mail address: deendarlianto@ugm.ac.id (Deendarlianto).

https://doi.org/10.1016/j.nucengdes.2023.112179
Received 3 November 2022; Received in revised form 9 January 2023; Accepted 18 January 2023

Nomenclature

Symbols

J_G	Gas superficial velocity (m/s)
J_{LD}	Discharge liquid superficial velocity (m/s)
x/L_H	Measurement location/locus (-)
Me	Mean/average (-)
Sd	Standard deviation (-)
Sk	Skewness/symmetry (-)
Ku	Kurtosis/flatness (-)
$A5$	Wavelet approximation (-)
$D1$	Wavelet detail (-)
ξ	Kolmogorov entropy (bits/s)

Abbreviations

CCF	Counter-current two-phase flow
CCFL	Counter-current flow limitation
PWR	Pressurized water reactor
SG	Steam generator
RPV	Reactor pressure vessel
PDF	Probability density function
PSDF	Power spectral density function
DWT	Discrete wavelet transform
ZLP	Zero liquid penetration
TOPFLOW	**T**ransient tw**O** **P**hase **FLOW**
HJ	Hydraulic jump

governing CCFL (Wongwises, 1994; Wongwises, 1996; Navarro, 2005; Badarudin et al., 2018a; Ma et al., 2020), and also the interfacial behaviors due to the applied flow parameters (Deendarlianto et al., 2005; Deendarlianto et al., 2011b; Vallée et al., 2012a; Lucas et al., 2017; Badarudin et al., 2016; Badarudin et al., 2018b; Astyanto et al., 2022a). Moreover, the effects of the fluid properties were also exhibited, but remained less significant. It comprised the influence of the liquid viscosity (Zapke and Kröger, 1996; Ghiaasiaan et al., 1997; Minami et al., 2010; Kinoshita et al., 2011, Prayitno et al., 2012; Astyanto et al., 2022b) as well as the surface tension (Deendarlianto et al., 2004; Deendarlianto et al., 2010; Ousaka et al., 2006) on the flooding characteristics in which the results exhibited unremarkable results. In addition, several computational works were also done during the development of validating data on its physical models (Deendarlianto et al., 2011a; Deendarlianto et al., 2012a; Utanohara et al., 2012).

From the view point of scaling parameters, the utilization of a large scale PWR hot leg typical geometry with a circular cross-section to investigate the flooding mechanisms was reported by Al Issa and Macián-Juan (2014), Al Issa and Macián-Juan (2017). Both were on the basis of detailed visual identifications of the high quality videography toward the transition mechanisms due to the fact that only few investigations were performed at large scales with detailed identification of flow patterns and the interfacial behavior during CCFL (Al Issa and Macián-Juan, 2011; Al Issa and Macián-Juan, 2014). Furthermore, another work focused on the transition mechanisms that contribute to CCFL by using computational fluid dynamic (CFD) validations during the transient condition which was further also conducted (Al Issa and Macián-Juan, 2017). On the other hand, devoted to the better optical measurement techniques for the better understanding through the visualization, the use of a large-scale simulator with a precisely flat channel with 250 mm × 50 mm of cross-sectional area to conduct transient CCFL experiments with a pressure chamber to maintain the reactor simulator's operating pressure were reported by Deendarlianto et al. (2011b) and also Vallée et al. (2012b). Furthermore, Lucas et al. (2017) reviewed the previous obtained data utilizing new sophisticated measurement systems through a steady flow approach. Here, several cameras were applied to detect the fluid interfacial dynamics during CCFL while the data tabulation involved both the air/water and steam/water experiments. During their works, another transformation of the qualitative data into a quantitative validation during the development of the CFD model through image processing procedures was strongly suggested due to the fact that the present CFD approach has not met the high confidence's level in the field of reactor safety involving complex two-phase flow structures (Lucas et al., 2016). However, during the flooding mechanisms' investigations, particular authors also made several measurements including the pressure gradient, and also the instantaneous either the water level or the void fraction behaviors. Here, the time-series pressure fluctuation's characteristics may indicate CCFL, while the void fraction represents the interfacial wavy movements. Actually, the utilization of either signal or image data processing enables those time-serial investigations.

In two-phase flow's measurements, a signal processing technique, enabling the physical-objective measurements, may involve either the resistive or capacitive concepts. On the other hand, the image processing commonly exhibits the development of modern optical instrumentation on capturing the flow phenomena. However, both techniques enable the time-serial data acquisitions which can undergo further analysis based on the domain of time and/or frequency. Furthermore, on the basis of the acquired signals, the points of regime transition (Zhang et al., 2010), covering amount of loss information along an attractor reflecting the units of real time (Johnsson et al., 2000), may be embedded during its chaotic analysis.

During the signal analysis based on its time-domain, an assessment through probability density function (PDF) is able to overcome the average of liquid thickness obtained from water level probes during CCF in both a 1/15 (Kinoshita et al., 2011) and 1/30 (Astyanto et al., 2022a) scaled-down PWR hot leg, and also the particular void fraction signal fluctuation behaviors during the slug identification in a horizontal conduit applying resistive probe (Rodrigues et al., 2020). Moreover, the PDF assessment during the quantification of the pressure fluctuations' signals gained more attention during either two-phase regimes' identifications or interfacial behaviors' characterizations (Jana et al., 2006; Catrawedarma et al., 2021a; Catrawedarma et al., 2021b; Astyanto et al., 2021a; Astyanto et al., 2021b; Wijayanta et al., 2022). On the other hand, the analysis based on the domain of frequency, namely the power spectral density function (PSDF), enables the identification of flow structures during two-phase flow regime assessments by using the signal acquired from capacitance probes (Canière et al., 2007), the characteristics of liquid wave through horizontal conduits (Setyawan and Indarto, 2016; Hudaya et al., 2019; Wijayanta et al., 2022), the flow structure analysis on a vertical conduit on the basis of fluctuations of the differential pressure (Catrawedarma et al., 2021a), the slug behavior during CCFL by means of differential pressure probes (Lucas et al., 2017), and also the interfacial fluctuations on gas/liquid CCF on a small scale PWR hot leg typical geometry (Astyanto et al., 2022a). Here, the stratified, wavy, slug and annular flow as well as the regimes before and after CCFL obtain different spectrum characteristics.

From the view point of the time-frequency domain analysis, a signal variance decomposition through a wavelet transformation enables the fluctuation energy assessment of the flow. It was successfully conducted to identify the flow behaviors obtained from the conductivity signal of both co-current liquid-liquid flow in a vertical conduit (Jana et al., 2006), and also gas/liquid CCF obtained by parallel wire array probes in a model of 1/30 PWR hot leg (Astyanto et al., 2022a). Furthermore, it was reported to be performed in the flow pattern identification obtained by capacitance probes (De Kerpel et al., 2015) as well as the identification of the flow structure based on the void fraction obtained by impedance probes (Nguyen et al., 2010). Moreover, considering the differential pressure in a vertical conduit corresponds to the mean of volumetric void fraction, the flow regime was proposed to be completely identified through the characteristic vector from the wavelet variances (Elperin & Klochko, 2002). In addition, the energy distributions during flow structure assessments obtained by differential pressure probes on the airlift pump type microbubble generator (Catrawedarma et al., 2021a) and the interfacial behaviors on stratified co-current flow (Wijayanta et al., 2022) obtained by pressure differential probes were also successfully conducted. The above authors noticed that the wavelet energy distributions obtain certain trends depending on the flow regimes. Moreover, during a signal decomposition by utilizing a type of discrete wavelet transform (DWT), the flow regime clustering is able to be developed on the basis of Fuzzy C-Means algorithm (dos Reis & Goldstein, 2010). It was further reported that the cluster of the flow regimes is better established through the use of the wavelet signal decompositions as the input layer of an artificial neural network (Catrawedarma et al., 2021b). Here, particular authors reported that the obtained wavelet variance distributions correspond to the occurred flow regimes.

On the basis of chaotic analysis, a non-linear analysis, namely the Kolmogorov entropy, of the signals which were obtained from ring-type measuring electrodes to characterize the flow regimes was successfully applied (Jin et al., 2003). Moreover, it enables the measurement of the degree of unpredictability which was obtained from both differential pressure signals during the characterization of the flow structures on airlift pump system (Catrawedarma et al., 2021a), the identification of interfacial behaviors on co-current stratified flow (Wijayanta et al., 2022), and also water level fluctuation signals obtained by parallel wire array probes during the investigation of the interfacial fluctuations on gas/liquid CCF in the 1/30 model of the PWR hot leg (Astyanto et al., 2022a). Here, those authors strongly noticed that the Kolmogorov entropy of two-phase flow systems which also represents the chaotic level of the signal depends on either the gas or liquid superficial velocity.

Recently, image processing techniques have been extensively developed in which the extracted data are claimed to be able to quantitatively characterize the interfacial dynamics during the two-phase flow. Furthermore, it provides numerous advantages such as elaborating non-intrusive flow characterizations, the ease in calibration and also flexible deployment. The advancement of optical instruments and computer systems further enhance the evolution of this method as well. The techniques have been well proven to be dependable to obtain the data on the characteristics of interface (Montoya et al., 2012; do Amaral et al., 2013; Widyatama et al., 2018; Badarudin et al., 2018; Hudaya et al., 2019; Wijayanta et al., 2023) in gas/liquid flows. Herein, to obtain the interface fluctuations representing the water level dynamics, the algorithm employed by do Amaral et al. (2013), Widyatama et al. (2018), Hudaya et al. (2019) and also Wijayanta et al. (2023) were almost similar. The scripts were developed in which each frame obtained was converted to grayscale while the background was removed to obtain the interface. Moreover, the information of gas/liquid interface line is then transformed into either a void fraction or water film thickness. However, the developed techniques still leave room for an algorithm optimization in which both the computational time and accuracy need to be further improved.

From the aforementioned literature surveys, it is noticed that there are still challenges to propose an investigation on the statistical characterizations of the interface behaviors during CCF in a PWR hot leg geometry obtained from a novel image processing algorithm utilizing the videography materials. Furthermore, it has been projected to be able to transform more qualitative data to time-series quantitative parameters of either the local flow structure or interfacial behavior during gas/liquid CCF (Lucas et al., 2017). Since the technique involves a non-intrusive measurement, the obtained data may represent the better approaches due to the actual phenomena, and can further contribute to the development of CFD model validations. Therefore, the present work enriches the field of the interfacial behavior' studies in CCF during the effort to promote nuclear reactor safety through an optical-intrusive measurement, and provides an extensively statistical approaches to challenge the further development in the future machine learning during the flow structure prediction.

2. Research methodology

2.1. Outline of experimental apparatus and procedures

The experiments were conducted at the **T**ransient tw**O** **P**hase **FLOW** (TOPFLOW) facility of Helmholtz-Zentrum Dresden Rossendorf (HZDR). The experimental apparatus reproducing a primary circuit of German-Konvoi typical PWR with a down-scale of 1/3 is schematically depicted in Fig. 1. The main components comprise a test section representing the hot leg, a reactor pressure vessel (RPV) simulator (B19) at the lower end of horizontal channel, the inclined part of steam generator (SG) inlet chamber, and the SG separator tank (B20A and B20B) at the upper end of the inclined channel. Here, the hot leg cross section is flat with 250×50 mm^2 of area and 2245.5 mm of horizontal length, while the RPV simulator and SG separator tank are identical vessels with $600\times800\times1600$ mm^3 of volume. Both the horizontal section of the hot leg and the SG inlet chamber utilize transparent glass material on its sides to afford both optical observations toward the flow structures, and also the illumination supporting the visual recording. In order to keep the operating pressure close to the actual reactor pressure, the device was operated in a pressure chamber in which the pressure was supplied using either compressed air or nitrogen.

To capture the flow phenomena along the horizontal section of the hot leg simulator, two SYGONIX 43176S cameras with a maximum resolution of 1600×1200 pixels were installed. Here, a wide-angle lens (O-FB/2.8) was also applied into each device. During the data recording, 1280×720 pixels of high definition (HD) video resolution with a frame rate of 60 Hz was set. Furthermore, the recording took 60 s of time duration. In addition, a set of light emitting diode (LED) panels was used as a background to enhance a homogeneous illumination. The cameras were mounted in the pressure chamber, and protected from pressure damage by using a pressure-resistant case.

During the experiment, to ensure a safe operation of the test equipment and avoid stress corrosion, the experimental circuit was filled with demineralized water with 1 – 5 μSm/cm of electrical conductivity. Here during the pre-data collection, the test equipment was set to be free from air inclusions which probably could cause inaccurate measurement. Meanwhile, to avoid air inclusions during the experiments, the water was circulated in the apparatus with the TOPFLOW pressure chamber in an open condition to release the air inclusions into the atmosphere. The water was pumped into the SG separator until the water level reached the height of the SG inlet chamber and then flowed through the hot leg to the RPV Simulator tank. At the same time the airflow from the compressor was injected into the RPV simulator tank, flowed along the hot leg and entered the SG separator tank. In this condition, the air and water flowed counter-currently along the hot leg.

To obtain accurate data, at least 10 min were provided to reach constant operational parameters. After this time of period, the measurements were started. In this experiment, a high-speed camera captured images for 13 s on the SG inlet chamber, while two cameras recorded for 60 s on the horizontal hot leg, and the signals of pressure were recorded with a frequency of 10 Hz, also for 60 s. While the gas flow rate was gradually increased before CCFL occurs, the injected water mass flow rate was kept constant. Afterward, the water flow rate was increased, and the procedure was repeated again. This effect led to water retention on B20A section of the SG separator. As a result, the water flowed over the steel plate to the B20B section. Each volume of those tanks was controlled by a pump. Furthermore, the zero liquid penetration (ZLP), describing a condition where no condensate flows into the RPV during CCFL, was validated by observing the level of water in the horizontal section. During the ZLP, the area of hot leg near the RPV

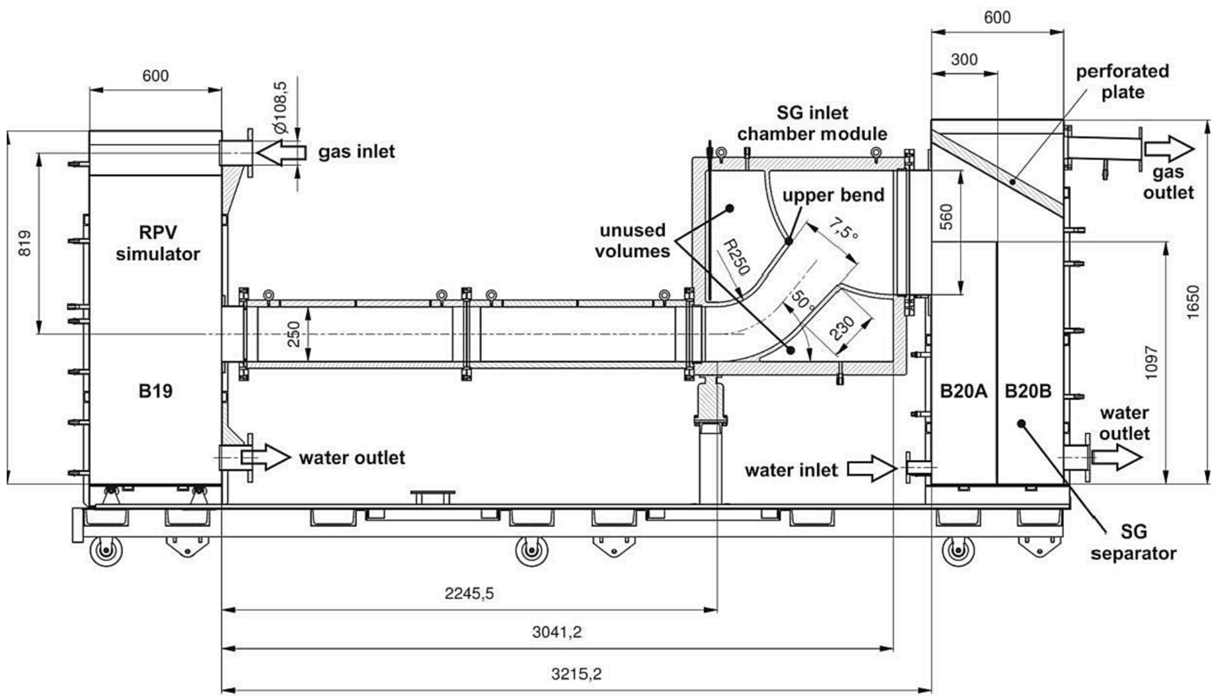

Fig. 1. The cut through the mid-plane of the experimental apparatus (Lucas et al., 2017).

simulator, approximately in the range of $0 < x/L_h \leq 0.1$, was free from water. Here, the water discharge to the RPV simulator was visually observed and physically verified by measurement using flowmeters which further enable direct determinations by a balance for the flow rate of the water withdrawn from the RPV simulator and the level change in the same tank as indirectly by a similar balance for the outer SG separator. It was also embedded with the pressure difference along the tank height. After ZLP, the gas flow rate was gradually declined and further CCFL data were recorded during de-flooding. After completing the first test series of water injection, this parameter was decreased to the next lower water flow rates. Every time of period of the test was equal for the above-mentioned procedure.

Moreover, the water/steam experiment was also conducted with the same procedure as the air/water flow. The difference in the steam/water experiment was that in the RPV simulator, the compressed air was replaced by saturated steam. In this experiment, the TOPFLOW pressure was higher than the air/water experiment. This aims to avoid steam condensation and interference the visual observation. The data collection during steam/water flow had the same procedures as the previous data collection on air/water flow, but with several additional instruments. Herein, during the steam/water flow, the heat losses along the feed line and in the test section were considered by a number of sensors. Therefore, an electrical heater circuit was further installed to support the line of steam through a cooler, a circulation pump, a heater, and a steam generator separator. In addition, associated transducers determined both the density and kinematic viscosity of the introduced steam.

Before data collection was carried out, the facility preheating, and both the SG separator and RPV simulators' activation were conducted. In addition, the test section was completely filled until the glass window was fully covered with water. Then, during the operation of circulation pump, the whole test section and circulation loop were continuously heated by an electric heater, which could supply up to 800 °C of temperature. To adjust and maintain the pressure, the TOPFLOW pressure chamber was filled with nitrogen gas, while the TOPFLOW steam generator supplied the steam. After the steam flowed into the simulator, the heater was turned off. Furthermore, typical information during the experimental procedures comprising the apparatus schematic, test section, sophisticated measurement techniques, and also working procedures in the data tabulation are detailed and described by Lucas et al. (2017).

2.2. Outline of image processing and data analyses procedures

In the present study, time-series water level fluctuations were obtained by means of a novel algorithm which is developed at Universitas

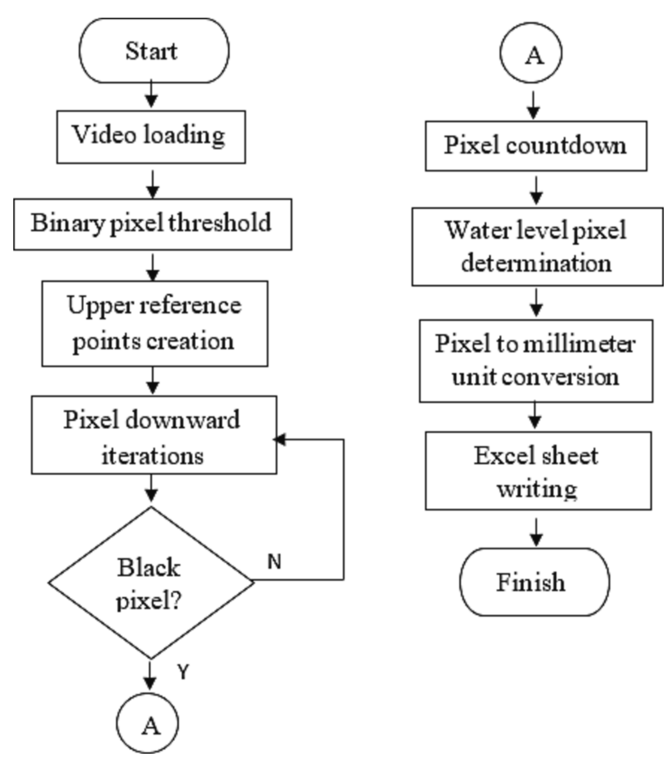

Fig. 2. The developed image processing algorithm used in the present study.

Gadjah Mada. Here, the developed image processing algorithm is described in Fig. 2. The setting of pixel ratio, image size, and video frame rate are possible to be adjusted through the syntaxes. In addition, the captured video can be directly processed without any separating step into image sequences. Furthermore, the visualization video is loaded into the script in order to extract it into the frames. Afterwards, the image pixel threshold determination is carried out. In this process, the frames are converted into binary images. The following stage is the void fraction pixel measurements which begins by determining the measurement reference points. It corresponds to the pixel distances from the upper reference which represents the top wall of the channel to the fluid interface. Next, the obtained void fraction pixels are converted to millimeters order by using the pipe height to pixel ratio. The interface which also represents the water holdup then is established as the ratio of the film thickness to the conduit height. Fig. 3 depicts the development of visual data during the image processing to obtain the interface fluctuations.

In addition, since the video material are in RGB color type, firstly the video is converted to a grayscale mode. The next process is image threshold determination. By this step, the contrast of the color is increased. Here, the darker colors are converted to black, while the lighter colors are converted into white. This aims to identify a contrast boundary between the water-air/steam interface. Here, the interface is then turned into black. The next step is setting the measurement references. These references show the starting and ending point for iteration from the top wall of the conduit to the fluid interface. As shown in Fig. 3 (c–e), a blue dotted line shows the origin while the green dotted line marked the ending point. Next, the script iteratively calculates the number of pixels as the distance from the origin to the interface.

Moreover, a set of the applied analysis parameters are tabulated as a test matriX arranged in Table 1. Both the mass flow rate and the system pressure were assessed as the analysis variables. Firstly, the water flow rate was kept as a constant parameter with various air flow rates. Here, 1,000 gr/s of a water flow rate and 570, 620 and 700 m^3/h of the air flow rates, respectively, were analyzed. Next, an air flow rate was kept constant with various water flow rates. Here, 700 m^3/h of an air flow rate and 1,000, and 2,000 gr/s of water flow rates were analyzed. The following involves both water and air flow rate to be kept a constant at 2,000 gr/s and 300 m^3/h, respectively, while both air/water at 1 bar and steam/water at 10 bars of system pressures were assessed.

On the other hand, another script on the basis of a commercial library was developed to identify the time-series interface dynamics representing the water holdup fluctuations. The data obtained were later analyzed through several statistical tools covering both stochastic and chaotic analyses. The stochastic analysis comprises the domain of both time and frequency, i.e., PDF and PSDF. Moreover, another time-frequency scale analysis obtained by the wavelet signal decomposition was exhibited to characterize the flow behavior due to the wavy interface. Additionally, the chaotic level of the system was also estimated on the basis of Kolmogorov entropy calculation. Those analyses were conducted with respect to the measurement locations, gas flow rates toward both the air/water and steam/water flow.

Table 1
Test matrix for the stochastic analysis.

Water mass flow rates (kg/s)	1			2
Pressure (bar)	1		1	10
Gas mass flow rates (m^3/h)	570	620	700	300

The stochastic analyses have been widely employed during either the flow regime identifications or the interfacial behaviors investigations on the basis of flow parameters in the horizontal channels (Canière et al., 2007; dos Reis & Goldstein, 2010), as well as the vertically positioned conduits (Jana et al., 2006; Ghosh et al., 2012; Ghosh et al., 2013), the effect of pipe orientation on CCF (Samal & Ghosh, 2020), and also the ratio of submergence of the micro-bubble generator which is embedded to an airlift pump system (Catrawedarma et al., 2021a; Catrawedarma et al., 2021b). Furthermore, the flow characterizations such as the water level behaviors, the occurrence of hydraulic jump and wavy interface are able to be evaluated through the signal quantification to obtain the moments of statistics covering the standard deviation, skewness and kurtosis (dos Reis & Goldstein, 2010; Wijayanta et al., 2022; Astyanto et al., 2022a). Moreover, a particular utilization of the cumulative PDF assessment may define the average liquid level (Kinoshita et al., 2011) and also the statistical characterization of the void fraction (Rodrigues et al., 2020). Moreover, a PSDF is proven to determine either the interfacial wavy movement or the flow pattern through its frequency distributions (Canière et al., 2007; Hudaya et al., 2019; Wijayanta et al., 2022; Astyanto et al., 2022a).

The PDF may quantify the signals in a time-domain flow regime identification. The amplitude of the signal is then expressed by its standard deviation and formulated as shown in Eq. (1) (Johnsson et al.,

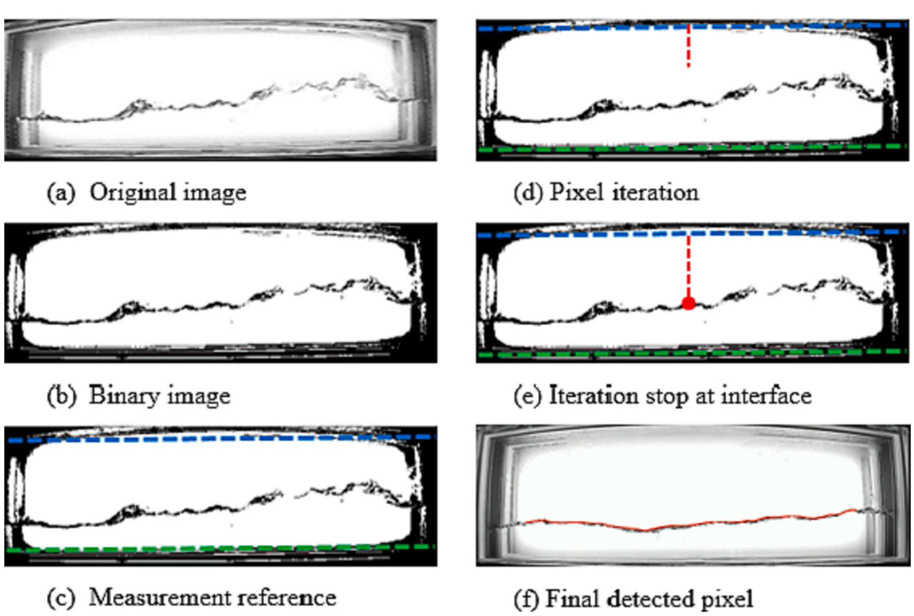

Fig. 3. Visualization steps of the image processing.

2000).

$$Sd = \sqrt{\frac{1}{N-1}\sum_{n-1}^{N}(x(n) - Me)^2} \quad (1)$$

Here in the Eq. (1), the mean, *Me*, represents the average of the data set and is formulated as shown in Eq. (2).

$$Me = \frac{1}{N}\sum_{n-1}^{N}x(n) \quad (2)$$

Moreover, the normalized third and fourth statistical moments of the distribution curve namely the skewness, *Sk*, representing the symmetry of a distribution curve, and kurtosis, *Ku*, which corresponds to the flatness of the curve, are expressed in a non-dimensional form as shown in Eqs. (3) and (4), respectively.

$$Sk = \frac{1}{NMe^3}\sum_{n-1}^{N}(x(n) - Me)^3 \quad (3)$$

$$Ku = \frac{1}{NMe^4}\sum_{n-1}^{N}(x(n) - Me)^4 \quad (4)$$

Additionally, Jana et al. (2006) remarked that a random variable with a cumulative distribution which is differentiable exhibits a PDF which is formulated as expressed in Eq. (5)

$$PDF = f(x_1, x_2, x_3, \cdots, x_n) = \frac{\partial^n F(x_1, x_2, x_3, \cdots, x_n)}{(\partial x_1, \partial x_2, \partial x_3, \cdots, \partial x_n)} \quad (5)$$

On the other hand, the PSDF which comprises the frequency-domain signal analysis through a fast fourier transform, may correspond to the occurrence of the wave's formation which can be physically recognized through its frequency. Here, the highest magnitude of the occurrence represents its dominant frequency. Furthermore, the power spectrum segment, $P^i_{xx}(f)$, determined as a sub-spectra number by reducing the acquired signal's variance, divides the time-series into L segments with individual length, N_s, and formulated as expressed in the Eq. (6) (Johnsson et al., 2000; Catrawedarma et al., 2021a).

$$P^i_{xx}(f) = \frac{1}{N_s U}\left|\sum_{N=1}^{N_s} x_i(n) w(n) exp(-j2\partial fn)\right|^2 \quad (6)$$

Here in the Eq. (6):

$$x_i(n) = x(n + iN_s) i = 1, 2, \cdots, Ln = 1, 2, \cdots, N_s \quad (7)$$

In the window's function, *w(n)*, the normalized spectrum by the power's factor, U, is expressed as written in the Eq. (8).

$$U = \frac{1}{N_s}\sum_{N=1}^{N_s} W^2(n) \quad (8)$$

Then, the average of power spectrum, $P_{xx}(f)$, is then expressed by Eq. (9).

$$P_{xx}(f) = \frac{1}{L}\sum_{i=1}^{L} P^i_{xx}(f) \quad (9)$$

The wavelet spectrum, representing the fluctuation energy, is proven to be utilized as flow structure characterization (De Kerpel et al., 2015; Catrawedarma et al., 2021a). It may be treated as the variance decompositions into scales, in the same way as the PSDF is the variance decomposition into the frequencies. Here, the spectrum of the wavelet decompositions is able to characterize the regimes accurately in which the variances' vector was proposed as the characteristic vector (Elperin & Klochko, 2002). Furthermore, on a flow structure clustering based on the machine learning, the usage of the energy distribution as the input layer established better predictive results than the moment of statistical parameters (Catrawedarma et al., 2021b). Moreover, in a time-domain analysis involving a multiresolution approach, the wavelet transform may reduce the sparsity up to 40 % on the average of the signal (Elperin & Klochko, 2002).

In addition, DWT, exhibiting a time scale-frequency analysis, may reveal the characteristic of signals (Elperin & Klochko, 2002; Zhang et al., 2010; Wijayanta et al., 2022). It is further formulated as shown in Eq. (10).

$$f(t) = \sum_{k \in Z} A_{J_2,k}\varphi_{J_2,k}(t) + \sum_{J=J_1+1}^{J_2}\sum_{k \in Z} D_{J,k}\Psi_{J,k}(t) \quad (10)$$

Here in the Eq. (9), the mother wavelet representing the signal approximation in the largest time-scale, $A_{J_2}f(t)$, is formulated as shown in the Eq. (11).

$$A_{J_2}f(t) = \sum_{k \in Z} A_{J_2,k}\varphi_{J_2,k}(t) \quad (11)$$

While the wavelet children which corresponds to signal detail in smaller time-scales, $D_J f(t)$, is formulated as shown in the Eq. (12).

$$D_J f(t) = \sum_{k \in Z} D_{J,k}\Psi_{J,k}(t) \quad (12)$$

In a simpler form, the Eq. (10) may be rewritten as expressed in Eq. (13).

$$f(t) = A_{J_2}f(t) + \sum_{J=J_1+1}^{J_2} D_J f(t) \quad (13)$$

3. Results and discussions

3.1. Flooding mechanisms

A visual observation my means of camera recording is occasionally conducted to observe the phenomena during the two-phase flow. Although it is reported as a subjective manner, the utilization of this method has been extensively reported by notable authors to investigate the flow structures during CCF (Mayinger et al., 1993; Wongwises, 1994; Choi & No, 1995; Zapke and Kröger, 1996; Ghiaasiaan et al., 1997; Petritsch & Mewes, 1999; Gargallo et al., 2005; Deendarlianto et al., 2010; Deendarlianto et al., 2011b; Prayitno et al., 2012; Vallée et al., 2012a; Al Issa and Macián-Juan, 2014; Al Issa and Macián-Juan, 2017; Lucas et al., 2017; Badarudin et al., 2016; Badarudin et al., 2018a; Badarudin et al., 2018b). Furthermore, it has often been designated as a non-intrusive method to investigate the flow behaviors. Additionally, numerous high quality images have been reported for their applicability to be engaged as the CFD validating materials (Al Issa and Macián-Juan, 2017; Lucas et al., 2017).

In the present work, a typical exemplary flow visualization with respect to the change of air flow rate on CCF under the condition of a constant liquid superficial velocity, $J_{LD} = 0.08$ m/s, at an atmospheric system pressure is described as depicted in the Fig. 4. Herein, Fig. 4(a) notices that at a low air velocity, $J_G = 10.8$ m/s, a stratified counter-current regime is observed. Here, a supercritical flow due to gravity with a rather wavy air/water interface which is indicated by a thin liquid film with a relatively small air stream disturbance is observed on the entire test section. This flow behavior indicates the occurrence of a stable CCF without hydraulic jump (HJ) as the transition from super-critical to subcritical flow. A close observation into the videography reveals that approaching the riser area, the wave performs a higher frequency due to the increase of the frictional force on the air/water interface. Therefore, the flow under this condition exhibits the entire regime of the stratified wavy flow. At the horizontal part of the hot leg, there is not significant change in water holdup due to deceleration of water flow. Similar phenomena were previously described by Deendarlianto et al. (2011b) as well as Vallée et al. (2012a) during the

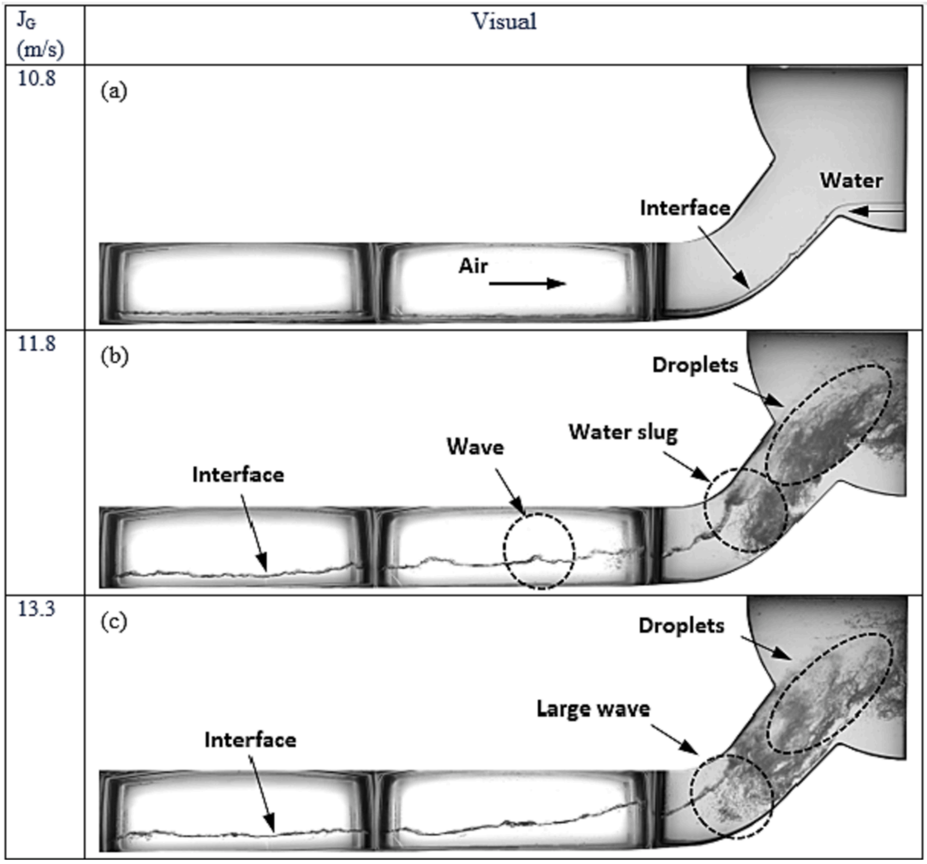

Fig. 4. Air/water flow visualization under the condition of J_{LD} = 0.08 m/s and (a) J_G = 10.8 m/s; (b) J_G = 11.8 m/s; (c) J_G = 13.3 m/s.

investigations of transient air/water CCF in a 1/3 model of PWR hot leg geometry, and also Al Issa and Macián-Juan (2014) during bend-CCFL with low air velocities on air/water experiment in a 1/3.9 downscaled of PWR hot leg model.

A stepwise increase in the air superficial velocity to J_G = 11.8 m/s leads to the increase of the friction on the air/water interface. It causes the water to decelerate, and the water holdup rises in the horizontal section. Furthermore, the increase of the air/water interface friction results in the flow to become wavier as shown in Fig. 4(b and c). Due to either the rise of water holdup or wave propagation in which its amplitude grows with droplet entrainment from its crest, the free cross-sectional area for the air flow declines, and accelerates the air velocity. It further begins to blow up the air/water interface and causes the wave to develop into either larger or roll waves. Next, this wave initiates a water blockage in the transition area near the riser. The observed phenomenon is in agreement to that previously reported by Deendarlianto et al. (2011b) in which the inception of flooding coincides with the liquid blockage representing the slug formation. Moreover, further increase in air velocity to J_G = 13.3 m/s increases the slug intensity and causes the slug level to reach the upper wall of the conduit. Physically, the phenomenon of slug-churn flow in the riser is due to narrowing the airflow cross-section during flooding. The narrowing of the cross-sectional airflow will accelerate the air on the wave's surface, causing the liquid slug to break into dispersed structures, i.e. bubbles and droplets.

In general, it is also noticed that CCFL begins with the appearance of waves flowing in the opposite direction of the water flow in which a gradual increase in the gas flow rate which causes the waves to grow in size with time. Furthermore, some waves turn into either large or roll waves and develop into a water blockage almost in the inclined section, and thus forms a liquid slug. This particular phenomenon confirms that previously reported by Lucas et al. (2017). Here also, droplets are generated at the crest of the waves and carried by the air flow through the riser to the SG separator tank. A further increase in the air flow rate causes the intensification of the blockage. The observed flooding phenomenon, again confirming the finding by Lucas et al. (2017) through the videography, is in good agreement also with those noticed by Deendarlianto et al. (2011b), Al Issa and Macián-Juan (2014), and also Badarudin et al. (2018b).

Fig. 5 depicts another typical visualization at J_{LD} = 0.16 m/s and J_G = 5.7 m/s for both the air/water and steam/water flows. From Fig. 5(a and b), it can be seen that in the horizontal section of the hot leg before CCFL, the flow obtains a wavy regime. Here, the water holdup tends to rise with the location shifts to the bend region. As a result, the gas flow is accelerated and generates roll waves. They become unstable with respect to the location, and break up into droplets which are carried upward the riser to the SG separator tank by the gas. This breaking of the roll wave due to the friction indicates CCFL. Moreover, both the air/water and steam/water flows reveal that CCFL occurs in the horizontal region. Here, the flooding mechanism at both system pressures obtains no significant difference. The observed flooding phenomena, which also confirm the visual report by Lucas et al. (2017), are in a good agreement with those noticed by Deendarlianto et al. (2011b) during a transient investigation on the same test facility.

Additionally, Figs. 6-9 present the typical time-tracing of both the air/water and the steam/water flows for the left and right cameras at J_{LD} = 0.16 m/s and J_G = 5.7 m/s. They quantitatively illustrate the flow developments supported by the visual materials in detailed descriptions with respect to the time-location investigations. From the figures, the characteristics of the wave growth can be sufficiently noticed. Here it can be also seen that at x/L_h = 0–0.48, the wave develops into a roll wave. Due to the friction of the air/water interface, the air flow breaks the roll wave. A close visual observation also shows that there is no blockage on the channel cross sectional area during the break of the roll wave as depicted on Fig. 6. Further observation at x/L_h = 0.53–1 shows

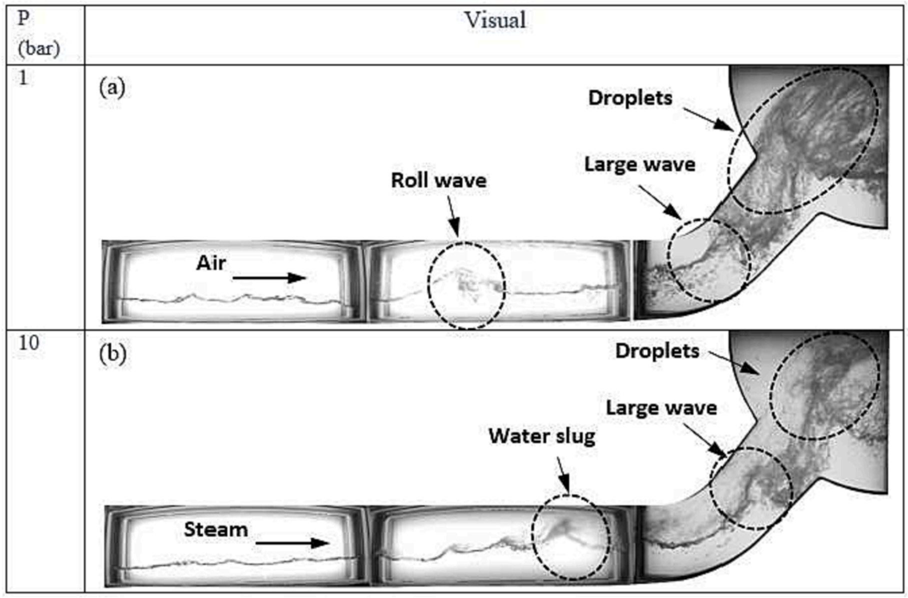

Fig. 5. Flow visualization at J_{LD} = 0.16 m/s; J_G = 5.7 m/s for (a) air/water flow at 1 bar; (b) steam/water flow 10 bars of system pressure.

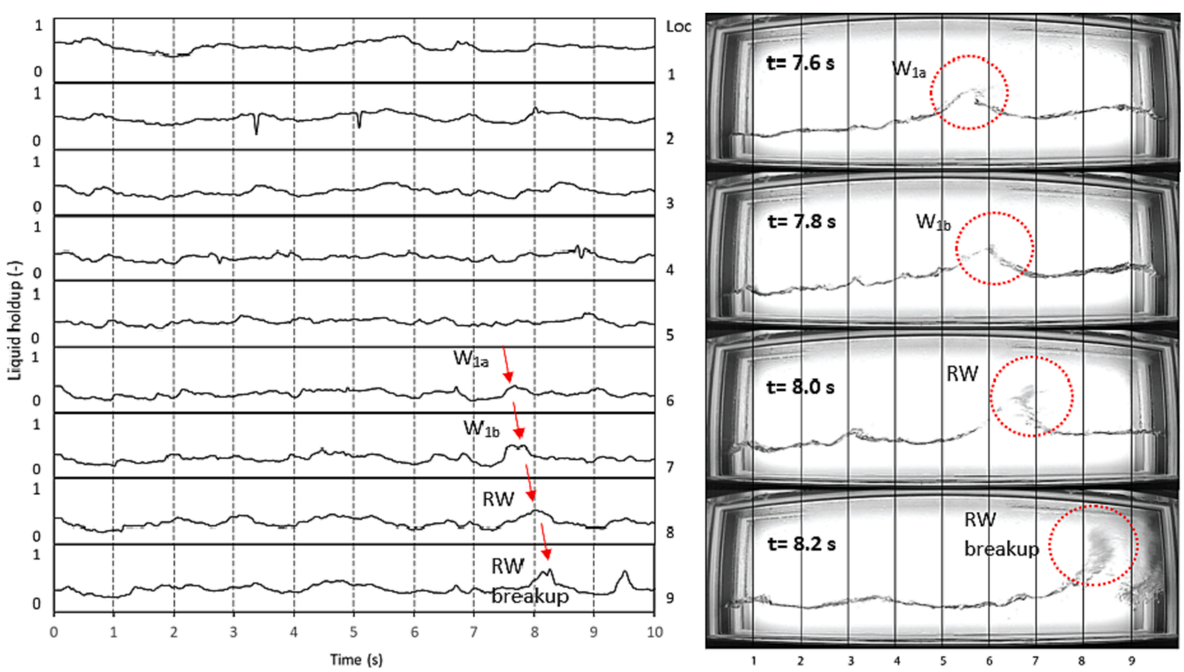

Fig. 6. Time-tracing interface fluctuations of the air/water flow at J_{LD} = 0.16 m/s; J_G = 5.7 m/s and 1 bar of system pressure on camera left-camera.

an increase in the water level along the pipe due to the interfacial friction in which the formation of a roll wave triggers the initial blockage and slug that reaches the top wall of the horizontal channel as shown in Fig. 7.

Moreover, from the flooding mechanism for the steam/water flow, it is revealed that a similar mechanism is obtained during this flow to the air/water at 1 bars of the pressure system. It starts with a wavy flow growing into a roll wave and further blocks the entire cross section. Close observations also notice that the water holdup is lower than that obtained with air/water flow. However, due to the higher pressure, the gas density increases. Besides, at x/L_h = 0–0.48, only a wavy flow appears, while at x/L_h = 0.53–1, the water blockage and slug appear similar to that obtained with air/water flow as shown in Fig. 8 and Fig. 9. This present finding emphasizes what also previously described by Deendarlianto et al. (2011b) in which the experiments, conducted both in transient and steady, obtain no significant difference on the flooding mechanisms.

3.2. Time and frequency domain analyses

A typical time and/or frequency-domain analysis of the air/water interface fluctuations using both the PDF and PSDF under the flow condition of J_{LD} = 0.08 m/s with respect to the change in air flow rate at a measurement location closest to the bend region (x/L_h = 1) are depicted in Fig. 10. The figure reveals that at J_G = 10.8 m/s, inhibiting a low air flow rate, a near-stable interface fluctuation as shown in column (a) which forms a unimodal distribution curve corresponding to a high void fraction with a very low standard deviation representing a smooth

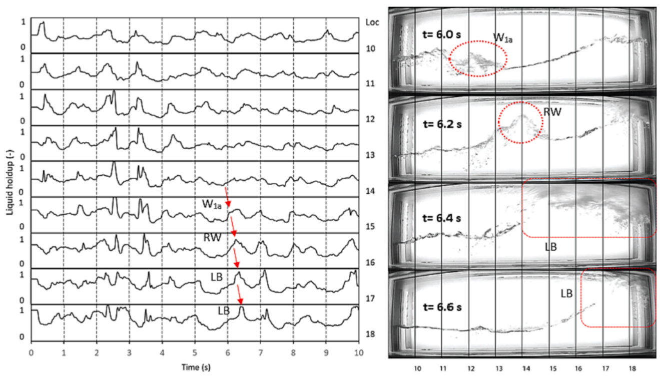

Fig. 7. Time-tracing of the interfacial fluctuations of the air/water flow at $J_{LD} = 0.16$ m/s; $J_G = 5.7$ m/s and 1 bar of system pressure on right-camera.

wavy interface as shown in column (b) are obtained. Here, the PSDF shows a medium-width band spectrum exhibiting a stratified flow. As the increase of the air flow rate, the maximum spectrum of the PSDF shifts to the lower frequency but in a higher magnitude as can be seen in column (c). At the lowest air velocity, the PSDF corresponds to the occurrence of the small waves, and it is noticed that the PSDF shows a high dominant frequency with a low magnitude.

Furthermore, when CCFL is reached, the PSDF later invites the occurrence of the liquid blockage as the slugs of liquid visibly replace the occurrence of the wave. In the PSDF, the maximum spectrum obtains a lower frequency but with a much higher magnitude (low frequency peak of large amplitude) in which it seems exponentially in its increase. Furthermore, it can be seen also that after CCFL is reached, as the air superficial velocity increases from $J_G = 11.8$ to 13.3 m/s, the maximum spectrum shifts to the lower frequency with the increase of the air velocity as shown in column (c). This means that the slug occurrence increases the air velocity increases. The obtained result confirms the report by Lucas et al. (2017) in which after CCFL was reached, the slug frequency on the basis of the pressure measurement along the horizontal section declines with the increase of the injected air flow rate.

Fig. 11 depicts another typical time-domain and frequency-domain analysis at $J_{LD} = 0.08$ m/s and $J_G = 13.3$ m/s with respect to the measurement locations. The figure notices that the interface visibly fluctuates in which the closest location to the bend exhibits the largest fluctuation as can be seen in column (a). Hence, a higher on both the average and standard deviation of the interface is exhibited as the location is closer to the bend as shown in column (b). Furthermore, the magnitude of the PSDF increases while the maximum spectrum tends to shift to the lower frequency along the location is closer to the bend region as shown in column (c). The possible reason of the current phenomenon is that there is an increase in the interfacial friction as the wave propagates in the upstream direction. Meanwhile, in the area of bend, as previously notified by Deendarlianto et al. (2011b) and also Vallée et al. (2012a), the recirculation of water as well as slug formation which involves bubble generation causes the waves propagate in both

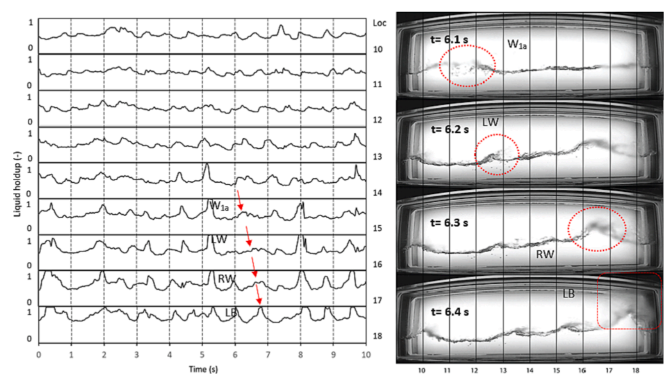

Fig. 9. Time-tracing of the interface fluctuations of the steam/water flow at $J_{LD} = 0.16$ m/s; $J_G = 5.7$ m/s and 10 bars of system pressure on right-camera.

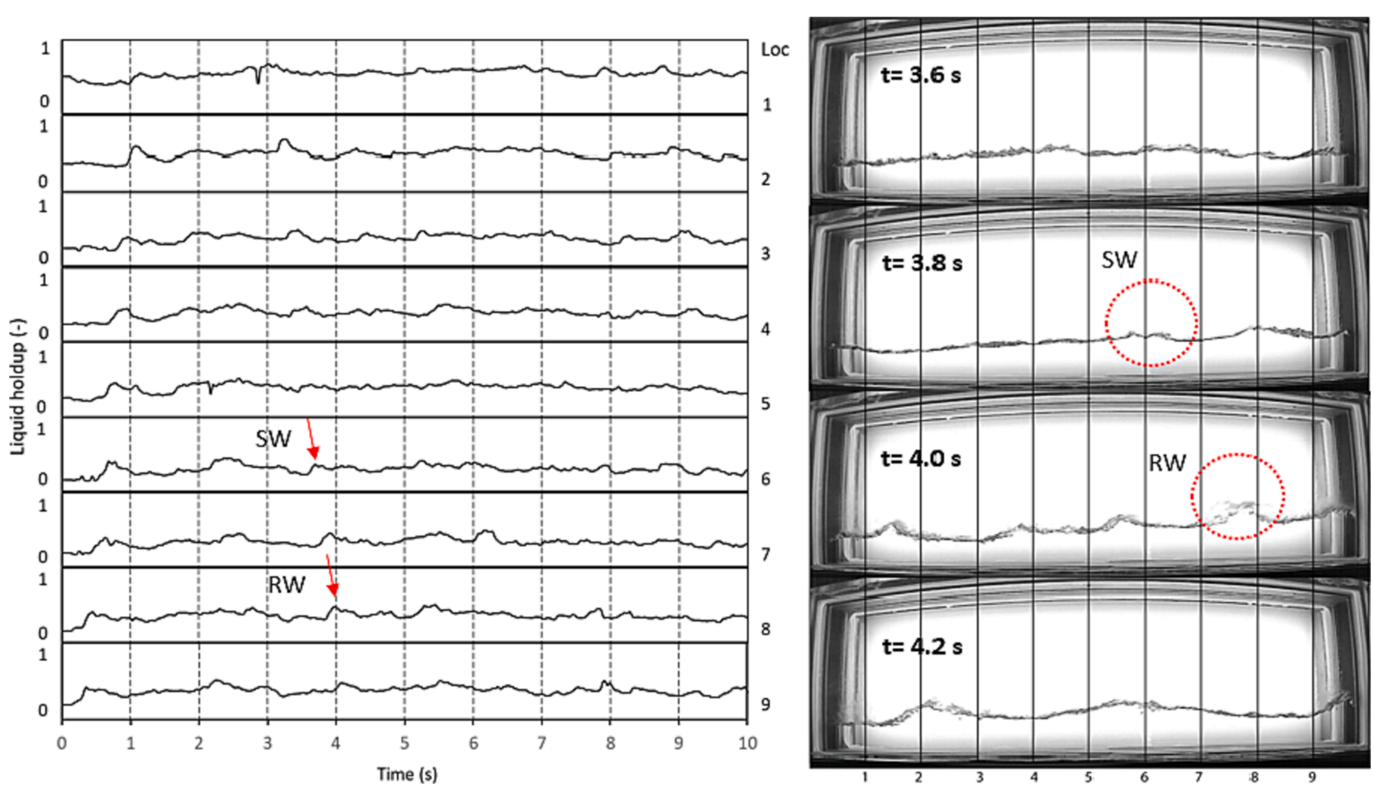

Fig. 8. Time-tracing of the interface fluctuations of the steam/water flow at $J_{LD} = 0.16$ m/s; $J_G = 5.7$ m/s and 10 bars of system pressure on left-camera.

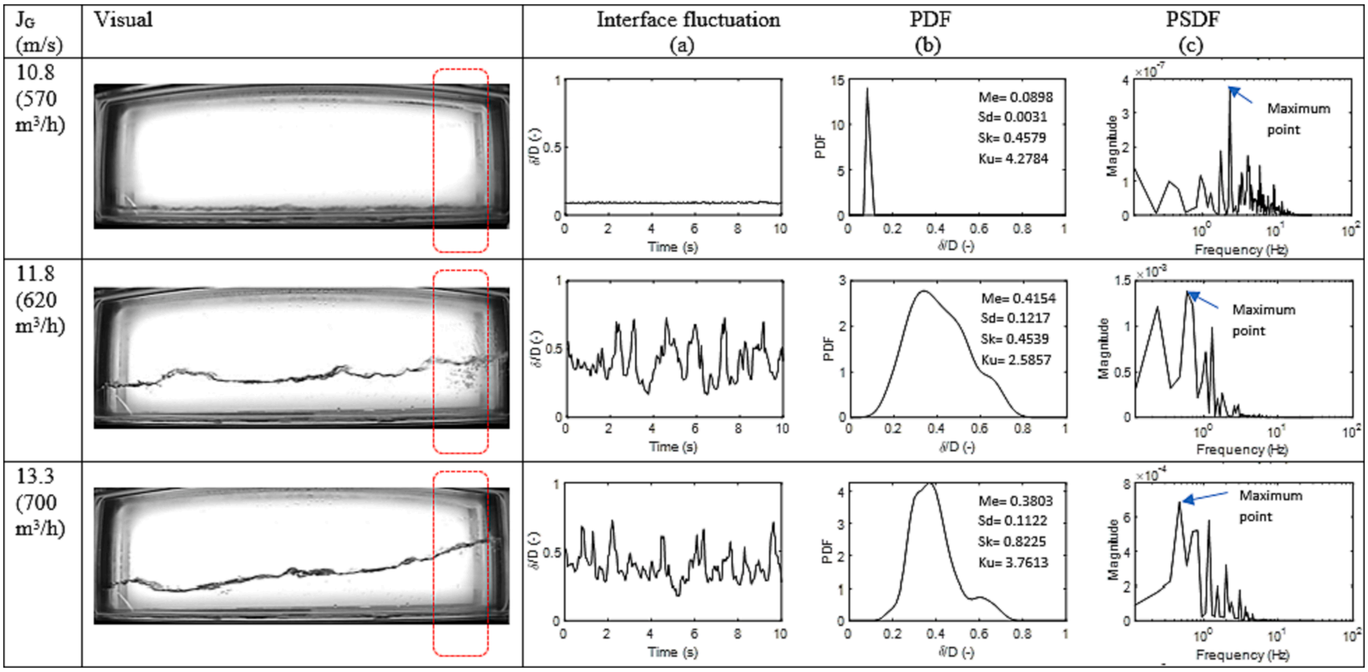

Fig. 10. Typical air/water interface fluctuations, PDF and PSD under $J_{LD} = 0.08$ m/s with respect to the air flow rate change at $x/L_h = 1$.

directions. It further explains why in the bend region the interface obtains the largest fluctuations with the most agitated flow region.

In addition, the average of water level under the flow condition of $J_{LD} = 0.08$ m/s is shown in Fig. 12(a). The figure reveals that a certain trend occurs for both $J_G = 11.8$ m/s and $J_G = 13.3$ m/s. Here, both averages increase as the location is closer to the bend. It further represents the water level increases in the upstream direction. The possible reason of this phenomenon is that the waves which are initiated in the downstream grow into either larger waves or roll waves as they propagate in the upstream direction, and later block the entire cross-sectional area of the conduit when they reach the bend as also exhibited by the visualization. Additionally, at half of the locations in the downstream, both $J_G = 11.8$ m/s and $J_G = 13.3$ m/s obtain almost equivalent water levels. On the other hand, at the lowest air velocity, $J_G = 10.8$ m/s, another trend is obtained. Here, the water level tends to very slightly increase as the location is closer to the bend region. Moreover, Fig. 12(b) shows the standard deviation of the interface under at $J_{LD} = 0.08$ m/s for various air velocities and locations. From the figure it can be seen that the standard deviation obtains a similar trend to the average. Here, both $J_G = 11.8$ m/s and $J_G = 13.3$ m/s reflect that the interface fluctuation increases as the location is closer to the bend region while the lowest air flow rate, $J_G = 10.8$ m/s obtains different trends in which the interfacial fluctuation decreases very slight as the location is closer to the bend region. Under the condition of $J_G = 10.8$ m/s, a very small fluctuation is obtained in comparison to that of the other air flow rates. A close visual observation reveals that a stable supercritical flow with a smooth interface is observed during this flow condition on the entire conduit. Here also, the acceleration of the water during its flow down from the SG separator results in a higher inertial rather than gravitational force.

Fig. 13 describes the typical interfacial fluctuations, PDF and PSDF at $J_{LD} = 0.16$ m/s and $J_G = 5.7$ m/s for the air/water and steam/water flows at the measurement location closest to the bend region, $x/L_h = 1$. The figure notices that high fluctuation interfaces with larger standard deviations are detected for both flow conditions as shown in columns (a) and (b). Here, the air/water flow obtains a higher fluctuation on the water level rather than the steam/water flow. Furthermore, it is interesting to be noted that the dominant spectrum shifts with very slight increase to the higher frequency while the smaller magnitude is obtained with the increase of the system pressure as shown in column (c). Again, the present finding confirms those previously reported Lucas et al. (2017), although the dependence of the slug frequency on the air discharge is very low. It is also confirmed that the slug frequency increases with the pressure, and decreases with the increase of the liquid discharge.

In addition, the average of the water levels under the conditions of $J_{LD} = 0.16$ m/s and $J_G = 5.7$ m/s with respect to the system pressure at various measurement locations are depicted in Fig. 14(a). From the figure, it is revealed that a different trend occurs for both system pressures. Here, the average tends to sharply decrease at $x/L_h = 0$–0.3 and increase at $x/L_h = 0.3$–1 during the air/water flow. It further represents the water level during the air/water flow. Although the visualization shows a similar flooding mechanism in which waves grow into a roll wave and further blocks the entire cross section, the air/water and steam/water exhibit different trends in the average of the liquid holdup along the horizontal section. Here, the water holdup obtained by steam/water is lower than by air/water flow. This might be caused by the different in pressure of those pairs of fluid flow. Since the gas density increases with the increase in its pressure, the steam later invites a higher density than the air, and therefore the liquid holdup during the air/water flow exhibits much lower in the average of the water holdup than the steam/water flow. On the other hand, the steam/water flow obtains a smooth increase as the location is closer to the bend region. It further shows the slight increase of the water level in the upstream direction.

Fig. 14(b) shows the standard deviations of the interface fluctuations under the flow condition of $J_{LD} = 0.16$ m/s and $J_G = 5.7$ m/s with respect to the measurement locations for both air/water and steam water flows at 1 bar and 10 bars of the systems pressure, respectively. From the figure it can be seen that the standard deviation shows a similar trend for both air/water and steam/water flows. It is noticed that the interface fluctuation gradually increases as the location is closer to the bend region while the location closest to the bend obtains suddenly an increase of fluctuation for the steam/water flow. A possible reason for this phenomenon is that the acceleration of the water during its flow down from the SG separator results in a higher inertial rather than gravitational force. Here, the bend region obtains the largest acceleration. Additionally, the steam/water flow correlates to a higher pressure rather than the air/water flow. It further affects both the density and

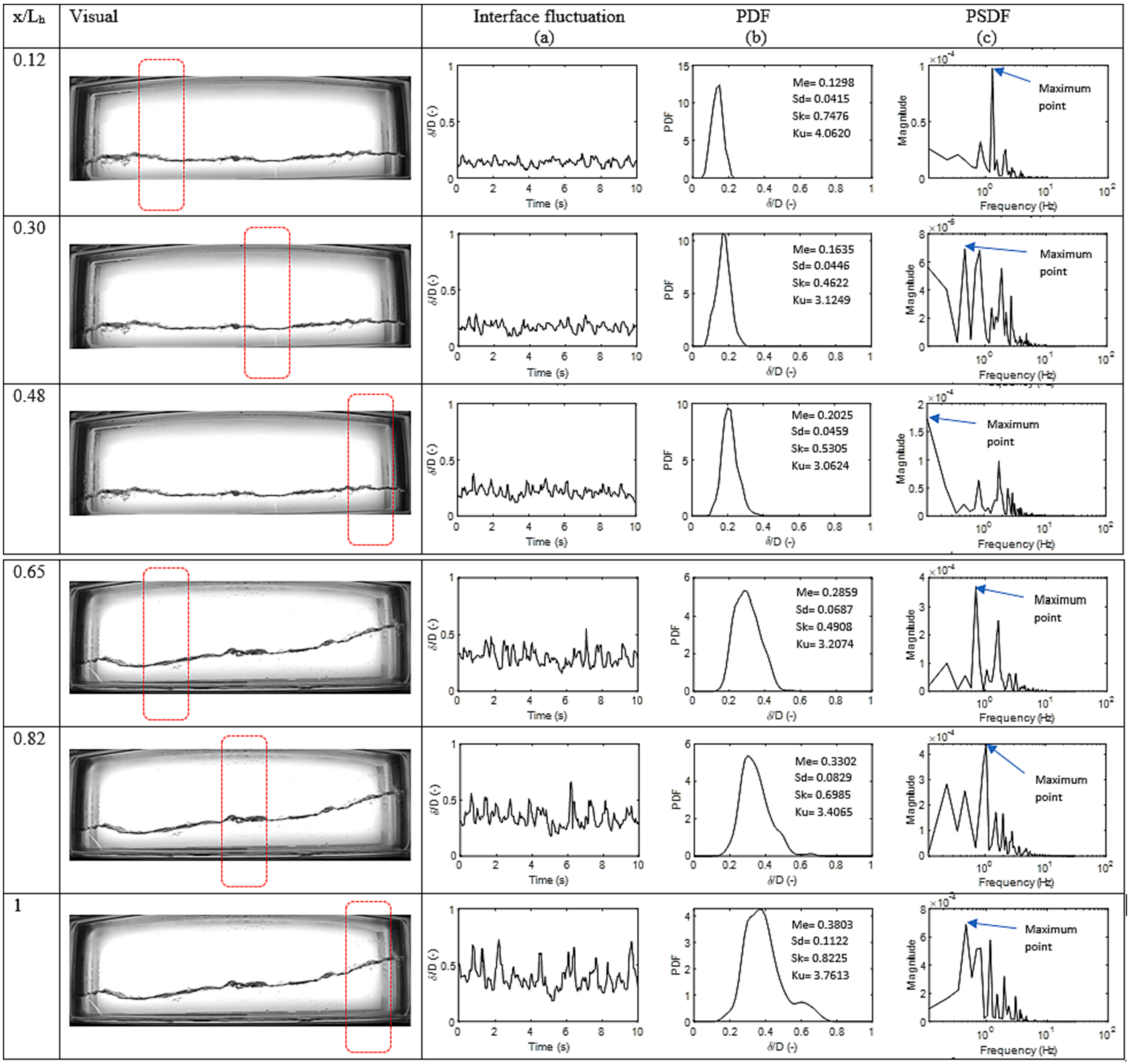

Fig. 11. Typical air/water interface fluctuations, PDF and PSD at $J_{LD} = 0.08$ m/s and $J_G = 13.3$ m/s with respect to the measurement location.

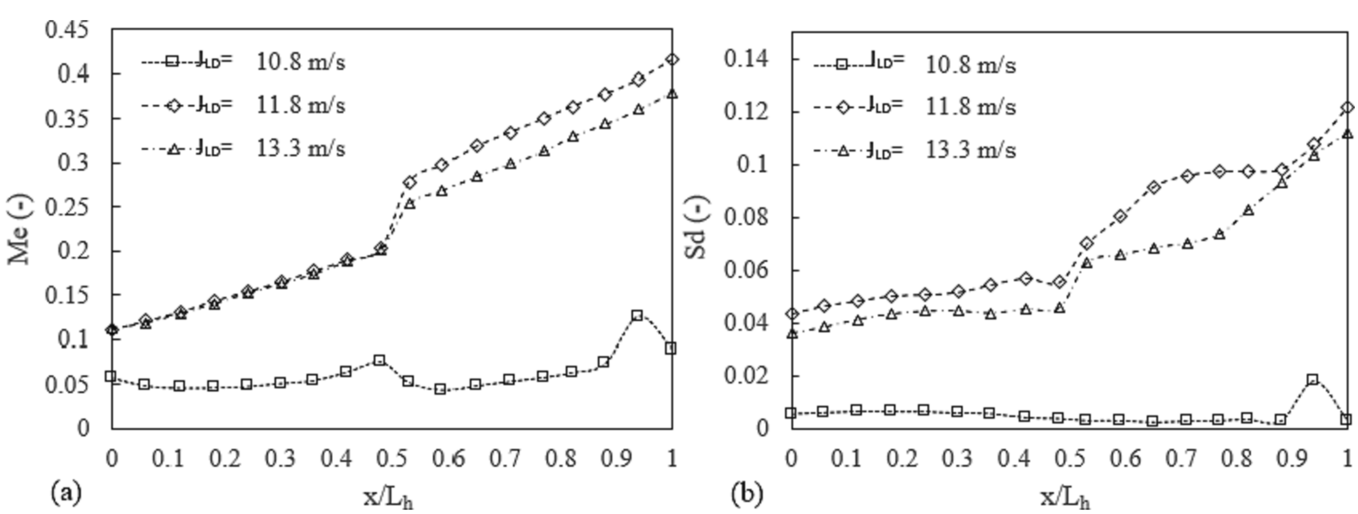

Fig. 12. The (a) average; (b) standard deviation of the liquid film thickness at $J_{LD} = 0.08$ m/s on various air discharges and locations.

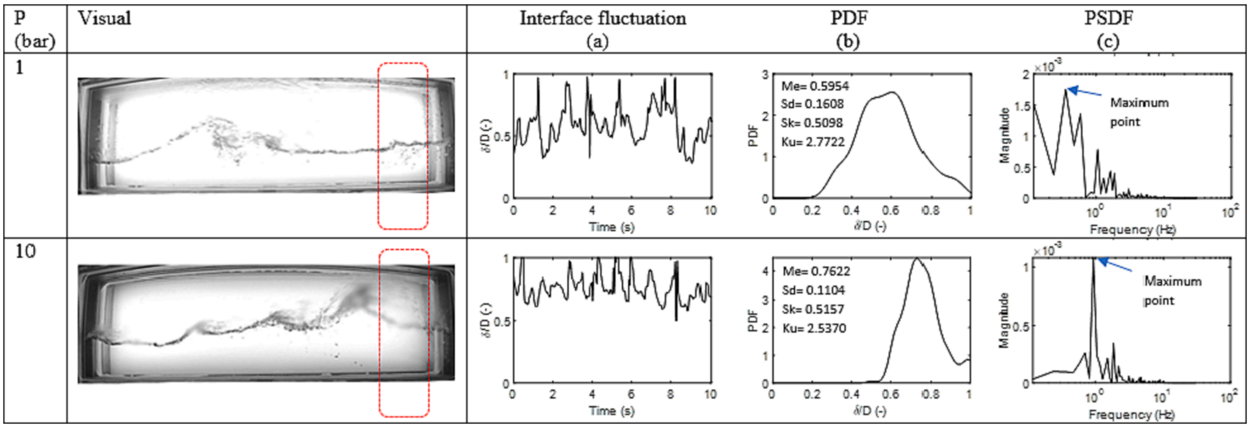

Fig. 13. Typical interface fluctuations, PDF and PSDF under $J_{LD} = 0.16$ m/s and $J_G = 5.7$ m/s at $x/L_h = 1$ for the air/water and steam/water flows.

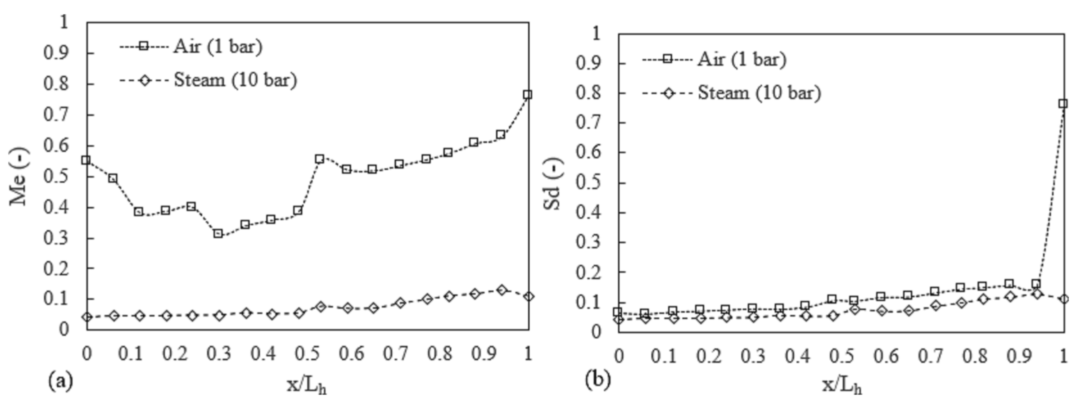

Fig. 14. The (a) average; (b) standard deviation of the liquid film thickness under the flow condition of $J_{LD} = 0.16$ m/s and $J_G = 5.7$ m/s with respect to the measurement location for the air/water and steam/water flows, respectively.

viscosity of the flow medium, respectively. Due the higher kinematic viscosity of the flow medium during the air/water flow, the higher interface fluctuation is then obtained. It results in the higher fluctuation obtained by the air/water flow. This phenomenon is in an agreement with the result which was previously reported by Kinoshita et al. (2011), and also Prayitno et al. (2012). In addition, due to the larger wall friction, the intensification of the slug was reported to increase with the decrease of the liquid viscosity (Utanohara et al., 2012).

3.3. Wavelet decomposition

In this investigation, a type of DWT, i.e. Daubechies 4 (db4), as previously also utilized by a number of researchers (Elperin & Klochko, 2002; Jana et al., 2006; Zhang et al., 2010; De Kerpel et al., 2015; Morshed et al., 2020; Catrawedarma et al., 2021a; Catrawedarma et al., 2021b; Wijayanta et al., 2022; Astyanto et al., 2022a) was employed to decompose time-series signals of the fluctuations of interface into five (5) levels with different frequency bands. Fig. 15 provides an exemplary typical decomposition at $J_{LD} = 0.08$ m/s and $J_G = 13.3$ m/s at the measurement location closest to the bend region, $x/L_h = 1$. In the figure, detail D1 corresponds to the highest frequency band with the smallest time-scale, while D2, D3, D4, and D5 obtain the lower frequency bands with higher time-scales, respectively. On the other hand, approximation A5 represents the largest-scale approximation with the smallest band of frequency. Thus, as proposed by Astyanto et al. (2022a) and also Catrawedarma et al. (2021a), as well as Jana et al. (2006), the approximation of signals, A5, may be investigated further to reveal the fluctuation characteristics due to the wave movements of the continuous interface.

A typical approximation and detail of the wavelet decomposition under the flow condition of $J_{LD} = 0.08$ m/s with respect to the change of the air flow rate at the measurement location closest to the bend region, $x/L_h = 1$, is shown in Fig. 16. The figure reveals that as the air flow rate increases from $J_G = 10.8$ m/s to $J_G = 11.8$ m/s, the larger amplitudes of the fluctuations of both the A5 and D1, respectively, are obtained as shown in columns (a) and (b). Here, the maximum wavelet variance, representing the fluctuation energy, shifts from a higher to a lower frequency band as can be seen in column (c). Further increase in air discharge from $J_G = 11.8$ m/s to $J_G = 13.3$ m/s exhibits a slight decrease on both the approximation and detail as depicted in columns (a) and (b), without being followed by a shifting of the frequency band of maximum energy as can be seen in column (c). Additionally, two trends of wavelet energy distribution as also shown in column (c) are obtained. They correspond to the different wavy interfacial characteristics during the flow. Before CCFL, the wavelet energy is distributed from D1 to D5 in which it obtains the highest variance in D3. It seems to correspond to the largest fluctuation energy which is obtained from the occurrence of either the large waves or the roll waves. On the other hand, when the inception of flooding is reached, the wavelet energy obtains a gradual increase from D1 to A5. It represents the largest fluctuation energy obtained from the liquid blockage which has a small frequency occurrence.

Fig. 17 depicts typical approximations, details and wavelet energy distributions under the flow condition of $J_{LD} = 0.08$ m/s and $J_G = 13.3$ m/s with respect to the measurement location. From the figure it is noticed that the closer the location to the bend, the higher the fluctuation's amplitude of both the approximation and the detail as depicted in columns (a) and (b), respectively. The possible reason of the corresponding phenomenon is that as confirmed also by the visualization

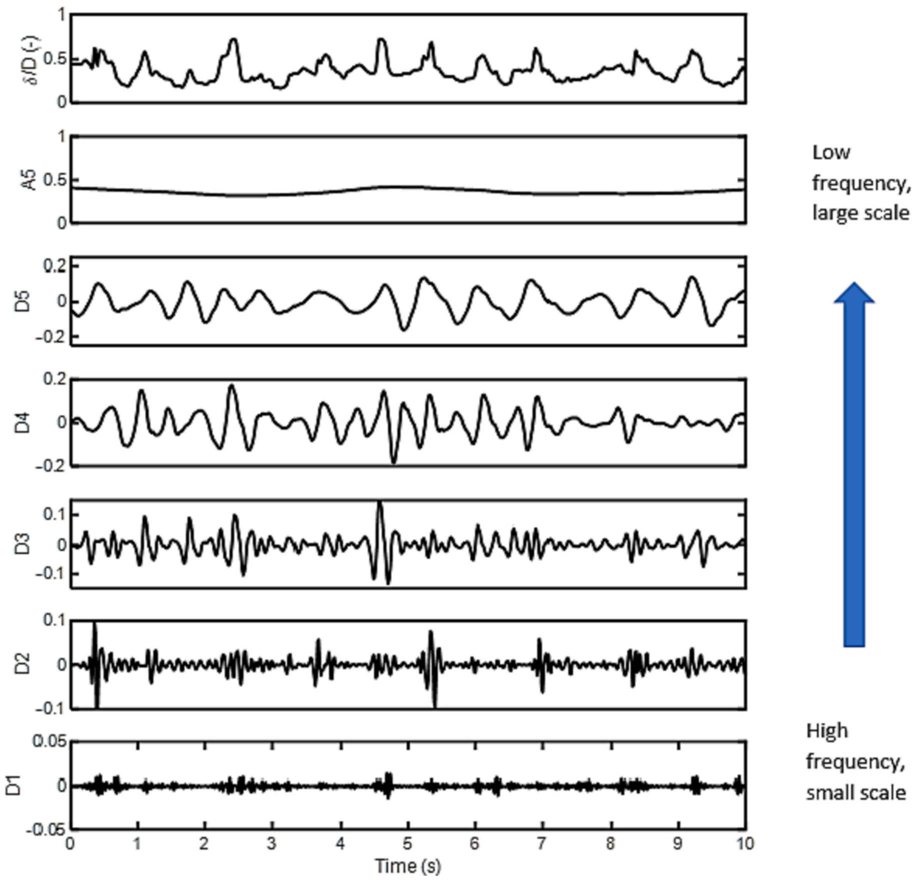

Fig. 15. Typical wavelet decomposition at $J_{LD} = 0.08$ m/s and $J_G = 13.3$ m/s at $x/L_h = 1$.

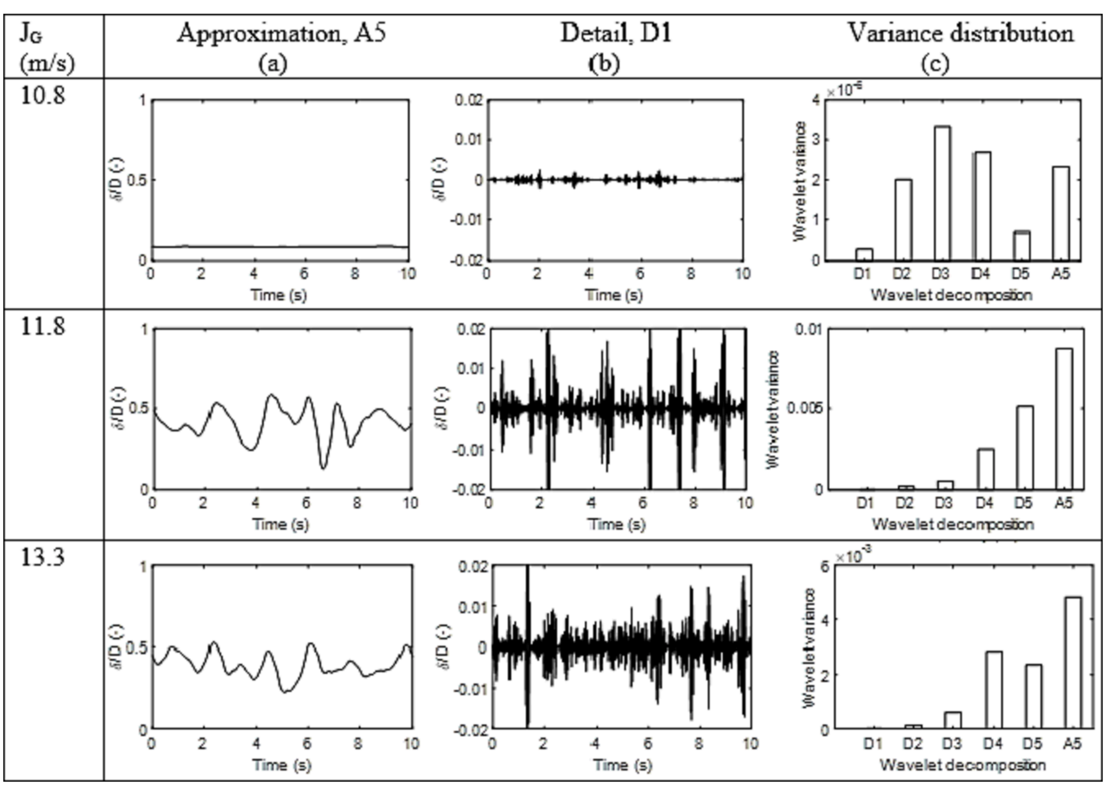

Fig. 16. Typical approximation, detail and wavelet variance of the water level fluctuations at $J_{LD} = 0.08$ m/s with respect to the air flow rate change at $x/L_h = 1$.

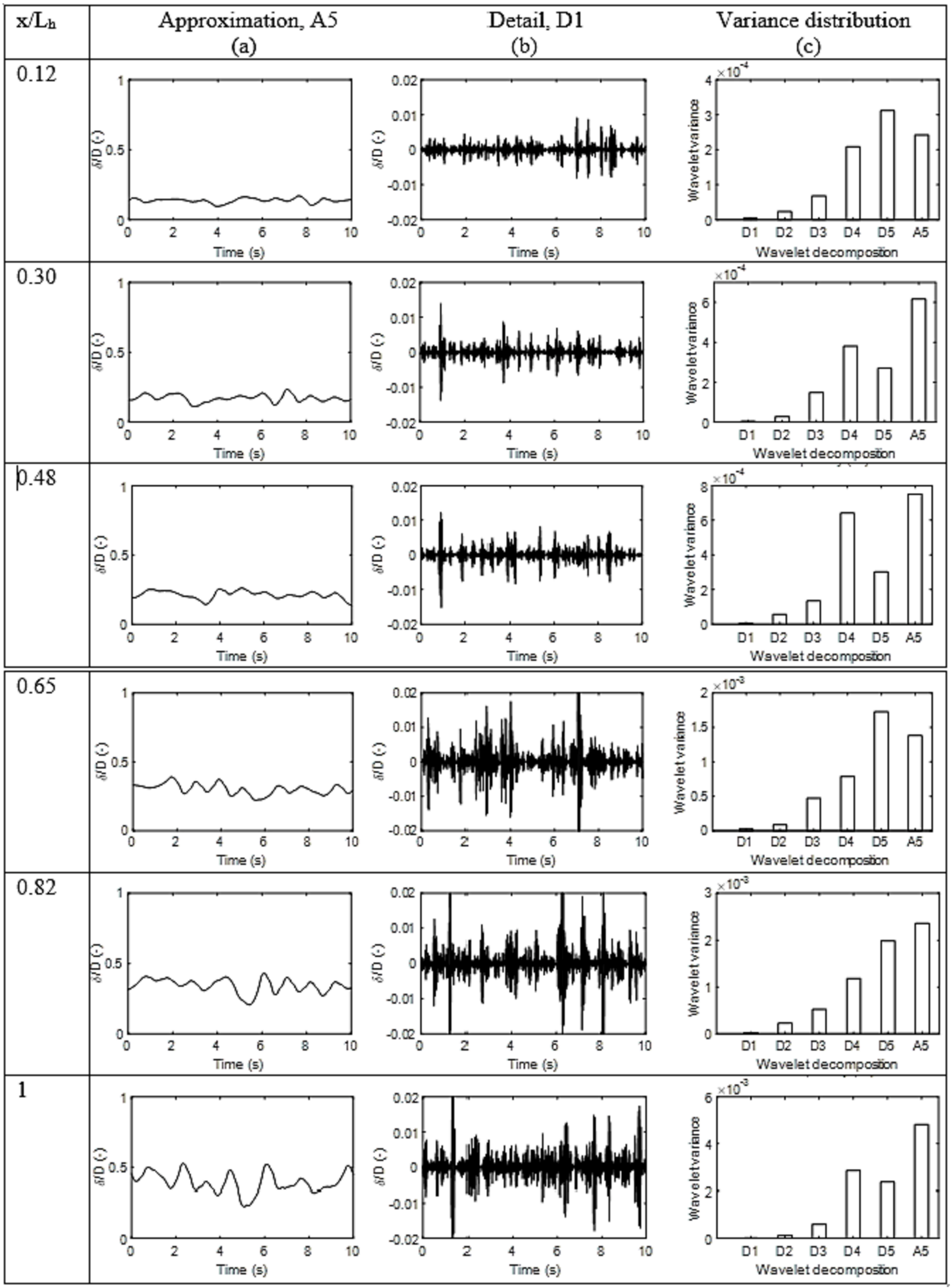

Fig. 17. Typical approximation, detail and energy distribution of the water level fluctuations at $J_{LD} = 0.08$ m/s and $J_G = 13.3$ m/s with respect to the measurement locations.

through video recording, approaching the bend, waves perform higher frequency due to the increase of the frictional force on the fluid interface. Besides, a recirculated region may be formed near the bend as a result of geometrical effect. In addition, a similar distribution trend of the wavelet variance as can be seen in column (c) corresponds to the relatively identical wave movements that occur during the flow. During the partial delivery regime, the wavelet variance obtains a gradual increase from D1 to A5. Moreover, Fig. 18 shows typical approximations, details and distribution of wavelet variance at $J_{LD} = 0.16$ m/s and $J_G = 5.7$ m/s at $x/L_h = 1$ for both air/water and steam/water flows, respectively. A close observation of the figure reveals that the air/water flow obtains higher amplitude of the fluctuations for both the approximation and the detail as shown in columns (a) and (b). Moreover, the wavelet variance tends to increase from the higher to the lower frequency bands. Here, the variance distribution reveals that the steam/water flow obtains a higher frequency but with a smaller magnitude on its maximum variance rather than the air/water flow.

In addition, Fig. 19(a) describes characteristics of the approximations at $J_{LD} = 0.08$ m/s at various measurement locations with respect to the change of the air velocity. It further corresponds to the wave dynamics which are obtained when the air discharge is stepwise increased. From the figure it is revealed that $J_G = 10.8$ m/s obtains a slight increase in the wavelet energy while its location shifts closer to the bend region. Hence, at both $J_G = 11.8$ m/s and $J_G = 13.3$ m/s, the wavelet energies tend to decrease while their location shifts closer to the bend area. The previous findings may reveal that the air flow rate obtains either unconcluded or unclear effects on the interfacial wave movements. Fig. 19(b) depicts another characteristic of the approximations under the flow condition of $J_{LD} = 0.16$ m/s, $J_G = 5.7$ m/s at $x/L_h = 1$ for both air/water and steam/water flow, respectively. They represent the interfacial wave movements which are obtained with respect to the system pressure change due to the different gaseous utilized.

Moreover, Fig. 19(b) implies that in both air/water and steam/water flows, the wavelet energy decreases as the location is closer to the bend region. Despite the system pressure having strong effects on the gas density, the fluctuation energy obtains a similar trend with the increase of the system pressure. It then reveals that the system pressure does not significantly change the characteristics of the wave movements. This finding is further in a partial agreement with Vallée et al. (2012a), as well as Ohnuki (1986), who reported that there were not essential differences observed during investigations for both air/water and steam/water CCF. Moreover, during this partial delivery, the increase of system pressure at a constant gas flow may result in more water to flow countercurrently with the gas, while a slightly increase in the system pressure occurs during the zero liquid penetration (Lucas et al., 2017).

3.4. Chaotic entropy

A chaotic analysis enables the investigation of the degree of unpredictability of a two-phase flow system due to the disturbances during the growth rate, in which a low entropy represents a regular information, while a higher entropy corresponds to the chaotic characteristics of a system (Catrawedarma et al., 2021a). The Kolmogorov entropy which is expressed in term of bits/second correlates the information loss during both an average time-cycle and real time (Johnsson et al., 2000). A nonlinear analysis of the signal entropy during the determination of the flow regime behavior was successfully reported by Jin et al. (2003). Besides, the investigation of information loss rate of the pressure fluctuation signal to detect transition points of the internal-loop airlift reactor was proposed by Zhang et al. (2010) through this entropy calculation. Furthermore, another measurement of the degree of unpredictability by using the Kolmogorov entropy was reported by Catrawedarma et al. (2021a) to investigate the effect of the gas discharge on the flow entropy. Currently, during the horizontal co-current stratified flow, the fluid physical properties was investigated to affect the flow entropy due to the stabilizing effect (Wijayanta et al., 2022) while the flow entropy corresponding to the randomly obtained characteristics due to the change of liquid velocity during gas/liquid CCF on a small-scale PWR hot leg geometry was also briefly assessed (Astyanto et al., 2022a).

In the present investigation, the Kolmogorov entropy of the fluctuations of interface at $J_{LD} = 0.08$ m/s with respect to the air flow rate change and the measurement locations is depicted in Fig. 20(a). From the figure it is revealed that both $J_G = 11.8$ m/s and $J_G = 13.3$ m/s obtain a similar trend. Here, the entropy slightly decreases with a relatively small fluctuation while the location is closer to the bend region. Furthermore, the lowest air flow rate, $J_G = 10.8$ m/s, despite its tendency to decline along the location is closer to the bend, the flow obtains a larger fluctuated entropy in comparison to the others.

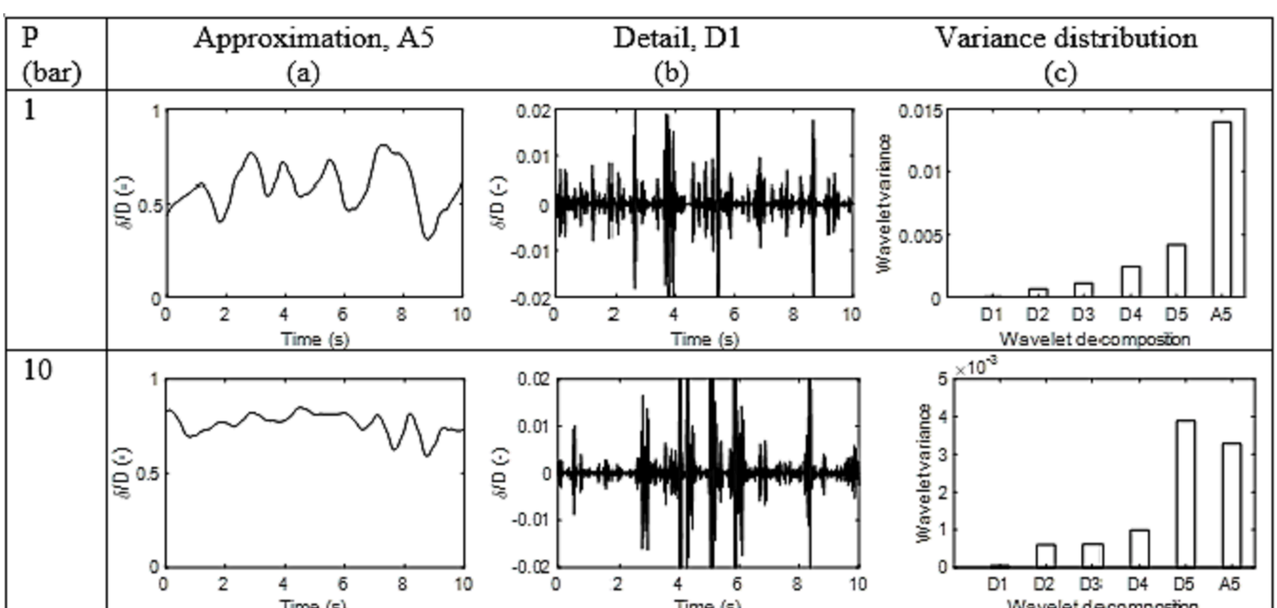

Fig. 18. Typical approximation, detail and wavelet variance of the water level fluctuations under the flow condition of $J_{LD} = 0.16$ m/s and $J_G = 5.7$ m/s at $x/L_h = 1$ for air/water and steam/water flows.

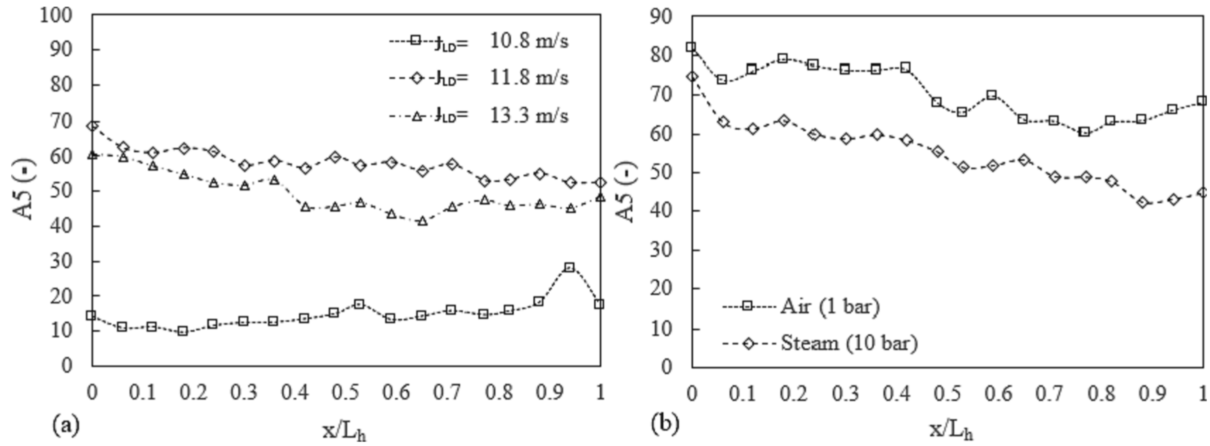

Fig. 19. The approximation of the energy fluctuation at (a) J_{LD} = 0.08 m/s with various air discharges; (b) J_{LD} = 0.16 m/s and J_G = 5.7 m/s with various system pressures.

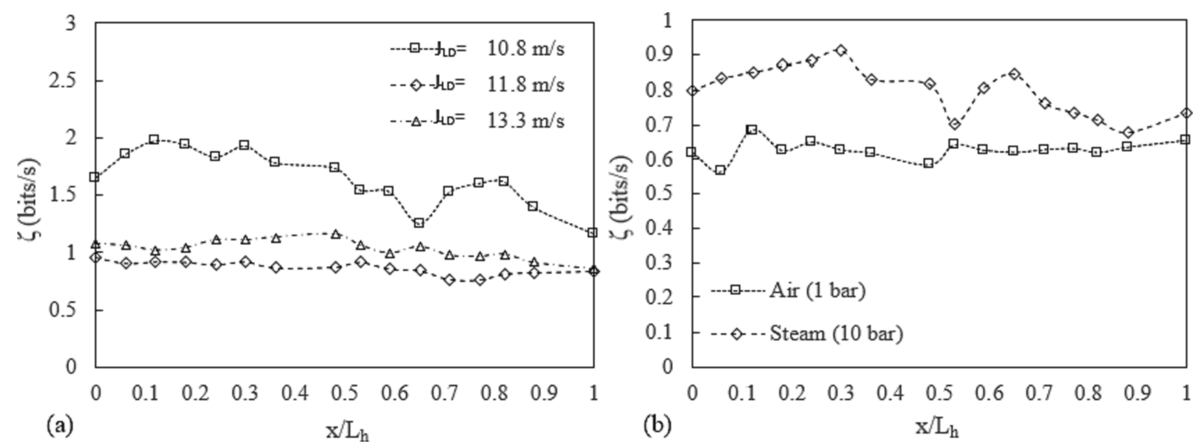

Fig. 20. The Kolmogorov entropy with respect to (a) the gas flow rates; (b) the system pressures at various measurement locations.

However, the figure also exhibits that this air flow rate obtains the highest entropy at the entire measurement locations. It later seems to correspond to the highest chaotic level with respect to the air discharge. From the visualization, it can be observed that during this flow condition, the air/water interface obtains a stable-wave performing a higher frequency due to the increase of the frictional force on the air/water interface during its location closer to the bend region. Here, there is also observed that the fluctuations in the water level due to deceleration of water flow are very smooth.

A further increase of the air flow rate leads to the increase on the friction of the air/water interface causing the water to decelerate, and the water level to rise in the horizontal section with a wavier interface. The air flow is thus accelerated, due to either the rise of water level or the wave in which its amplitude grows and results in the free cross-sectional area for the air flow to decrease. In the next second moment, the wave grows larger in size and develops into a roll wave due to interface disturbances caused by the air flow. This roll wave later initiates a water blockage in the transition area closer to the bend region. On the other hand, a further increase in air velocity increases the slugging's intensity. Physically, the phenomenon of slug-churn flow in the riser is strongly identified due to the narrowing of the airflow cross-section during the flooding. Moreover, it accelerates the air on the wave's surface, and causes the liquid slug to break into dispersed both bubbles and droplets. Al Issa & Macian (2014), through a detailed visual observation, reported that at the bend region both the turbulence and chaotic change of resistance was possibly obtained during the occurrence of CCFL due to the large blockages of the air path. Therefore, the present phenomenon may also be empirically correlated to the result obtained by Catrawedarma et al. (2021) who reported that the effect of the gas discharge on the entropy was very complicated due to different dynamic behaviors which are obtained by each of the flow regimes.

In addition, a typical Kolmogorov entropy characteristic of the interfacial fluctuations at J_{LD} = 0.16 m/s and J_G = 5.7 m/s for both the air/water and steam/water flows, respectively, is depicted in Fig. 20(b). From the figure it is noticed that both the air/water and steam/water flows obtain fluctuated trends. Here, the air/water flow obtains a higher entropy rather than the steam/water flow. A close visual observation reveals that the increase in the water level along $x/L_h = 0.53 - 1$ is clearly seen in which the formation of a roll wave triggers the initial liquid blockage which reaches the top wall. Meanwhile, for steam/water flow at 10 bars of the system pressure, it is also revealed that a similar mechanism is obtained in which a wavy flow starts, and grows up into a roll wave and creates blockage along the entire cross-sectional area of the conduit. Thus, the possible reason for this phenomenon is that since the steam/water flow correlates a higher pressure rather than the air/water flow, it further affects to both the density and viscosity of the flow mediums, respectively. Therefore, here a higher entropy seems to represent a higher fluctuation which is obtained by the air/water flow in which the higher the liquid viscosity, the larger the fluid resistance from internal forces acting to stabilize the interface fluctuation rather than the steam/water flow in which its lower viscosity exhibits a smaller stabilizing effect. This phenomenon is in an agreement to the results which were previously reported by Prayitno et al. (2012), and also Wijayanta et al. (2022).

4. Concluding remarks

A study was conducted to identify the behaviors of interface which are obtained by an image processing technique to the visual data during gas/liquid CCF on a large scale PWR hot leg. Statistical characterizations comprising time and/or frequency-domain analysis were carried out, and also embedded with its chaotic entropy to elaborate the behaviors of interface. Several remarks to be concluded are noticed as follows:

1. The flooding mechanisms are started with the appearance of waves which develop in size with the time along with the gradual increase of the gas flow rate, and later turn into roll waves and develop into a water blockage in the horizontal section close to the bend region. Here, the water level tends to rise with the location shifting closer to the bend region. As a result, the gas accelerates and generates roll waves. As the time proceeds, the waves become unstable with respect to the location, and break up into droplets which are carried upward to the riser to the SG separator tank by either the gas. The breaking of the roll wave due to the friction indicates CCFL. A further increase in gas discharge causes intensification of the water blockage.
2. The higher the pressure of system, the higher the frequency occurrence of slugging, while the injected gas flow rate obtained a different trend. However, the flooding mechanisms for both air/water and steam water flow obtain no significant difference. Moreover, both the air/water flow at 1 bar, and steam/water flow at 10 bar of the system pressures reveal that CCFL occurs in the horizontal region.
3. At high liquid flow rate, the wavelet variance, representing the fluctuation energy of signals, tends to decline as the location is closer to the bend. Both the air/water and steam/water flows exhibit the same trend. Before CCFL, the interface fluctuations remain smooth in which the wavelet variance distributes from the highest to the lowest frequency band. As CCFL is reached and followed by partial delivery, the regime is further characterized by fluctuations in the frequency and the occurrence of large wavy interfaces. Here, the wavelet variance gradually increases from the highest to the lowest frequency band.
4. The Kolmogorov entropy enables to correlate the stabilizing effect due to the fluid resistance which corresponds to either the system pressure or the fluid physical properties.

Declaration of Competing Interest

The authors declare that they have no known competing financial interests or personal relationships that could have appeared to influence the work reported in this paper.

Data availability

Data will be made available on request.

Acknowledgements

During the development of both the image processing algorithm and syntax, we are grateful for our application engineers, Mr. Muhammad Ardi Putra and Mr. Handaru Ramadhan Indira Darlianto, for their impressive works. We also appreciate Dr. Apip Badarudin, Mr. Arif Widyatama, and also Mr. Setya Wijayanta for their assistance during several brief discussions on either the optical image processing or the stochastic analyses. We proudly dedicate the present work to Mr. Muhammad Reza Pradecta's family. Herein, during the initial development on the image processing algorithm, Reza inspired us by performing his strong motivation as a team member on conducting this project. In addition, the experiments were carried out in frame of a research project funded by the German Federal Ministry of Economic Affairs and Energy, project number 150 1411.

References

Al Issa, S., Macián-Juan, R., 2011. A review of CCFL phenomenon. Annals of Nuclear Energy 38 (9), 1795–1819. https://doi.org/10.1016/j.anucene.2011.04.021.

Al Issa, S., Macián-Juan, R., 2014. Experimental investigation of countercurrent flow limitation (CCFL) in a large-diameter hot-leg geometry: A detailed description of CCFL mechanisms, flow patterns and high-quality HSC imaging of the interfacial structure in a 1/3.9 scale of PWR geometry. Nuclear Engineering and Design 280, 550–563. https://doi.org/10.1016/j.nucengdes.2014.08.021.

Al Issa, S., Macián-Juan, R., 2017. Image-processing of time-averaged interface distributions representing CCFL characteristics in a large scale model of a PWR hot-leg pipe geometry. Annals of Nuclear Energy 103, 282–293. https://doi.org/10.1016/j.anucene.2017.01.021.

Astyanto, A. H., Pramono, J. A. E., Catrawedarma, I. G. N. B., Deendarlianto, Indarto, 2022[a]. Statistical characterization of liquid film fluctuations during gas-liquid two-phase counter-current flow in a 1/30 scaled-down test facility of a pressurized water reactor (PWR) hot leg. *Annals of Nuclear Energy*, *172*, 109065. https://doi.org/10.1016/j.anucene.2022.109065.

Astyanto, A.H., Indarto, K., K. V., Deendarlianto,, 2022b. An experimental study on the effect of liquid properties on the counter-current flow limitation (CCFL) during gas/liquid counter-current two-phase flow in a 1/30 scaled-down of Pressurized Water Reactor (PWR) hot leg geometry. Nuclear Engineering and Design 399 (2), 112052. https://doi.org/10.1016/j.nucengdes.2022.112052.

Astyanto, A.H., Rahman, Y., Adhikara, A.Y., Indarto, D., 2021a. Time-series differential pressure fluctuations of a flooding regime : A preliminary experimental results investigation on a 1/30 down-scaled PWR hot leg geometry. AIP Conference Proceedings 060001 (2011).

Astyanto, A.H., Rahman, Y., Medha, A.Y.A., Deendarlianto, D., Indarto, I., 2021b. Pengaruh Rasio I/D terhadap Permulaan Flooding dan Fluktuasi Voltase Sinyal Tekanan Rezim Flooding pada Geometri Kompleks. Rekayasa Mesin 12 (2), 447–457.

Badarudin, A., Pinindriya, S. T., Yoanita, Y. V., Hadipranoto, M. S., Hartono, S., Ariawan, R., Indarto, Deendarlianto, 2018. The effect of horizontal pipe length to the onset of flooding position on the air-water counter current two-phase flow in a 1/30 scale of pressurized water reactor (PWR). *AIP Conference Proceedings 2001, 030011*(2018). https://doi.org/10.1063/1.5049983.

Badarudin, A., Indarto, D., Setyawan, A., 2016. Characteristics of the air-water counter current two-phase flow in a 1/30 scale of pressurized water reactor (PWR): Interfacial behavior and CCFL data. AIP Conference Proceedings 1737. https://doi.org/10.1063/1.4949303.

Badarudin, A., Setyawan, A., Dinaryanto, O., Widyatama, A., Indarto, D., 2018b. Interfacial behavior of the air-water counter-current two-phase flow in a 1/30 scale-down of pressurized water reactor (PWR) hot leg. Annals of Nuclear Energy 116, 376–387. https://doi.org/10.1016/j.anucene.2018.03.007.

Canière, H., T'Joen, C., Willockx, A., Paepe, M.D., Christians, M., Rooyen, E.V., Liebenberg, L., Meyer, J.P., 2007. Horizontal two-phase flow characterization for small diameter tubes with a capacitance sensor. Measurement Science and Technology 18 (9), 2898–2906.

Catrawedarma, I. G. N. B., Deendarlianto, Indarto, 2021. Statistical Characterization of Flow Structure of Air–water Two-phase Flow in Airlift Pump–Bubble Generator System. *International Journal of Multiphase Flow*, *138*, 103596. https://doi.org/10.1016/j.ijmultiphaseflow.2021.103596.

Catrawedarma, I. G. N. B., Resnaraditya, F. A., Deendarlianto, Indarto, 2021. Statistical characterization of the flow Structure of air–water–solid particles three-phase flow in the airlift pump–bubble generator system. *Flow Measurement and Instrumentation*, *82*(2018), 102062.

Choi, K.Y., No, H.C., 1995. Experimental studies of flooding in nearly horizontal pipes. International Journal of Multiphase Flow 21 (3), 419–436. https://doi.org/10.1016/0301-9322(94)00087-Z.

De Kerpel, K., De Schampheleire, S., De Keulenaer, T., De Paepe, M., 2015. Two-phase flow regime assignment based on wavelet features of a capacitance signal. International Journal of Heat and Fluid Flow 56, 317–323. https://doi.org/10.1016/j.ijheatfluidflow.2015.09.002.

Deendarlianto, Ousaka, A., Kariyasaki, A., Fukano, T., Konishi, M., 2004. The Effects of Surface Tension on the Flow Pattern and Counter-Current Flow Limitation (CCFL) in Gas-Liquid Two-Phase Flow in an Inclined Pipe. *Japanese Journal of Multiphase Flow*, *18*(4), 337–350.

Deendarlianto, Vallée, C., Lucas, D., Beyer, M., Pietruske, H., Carl, H., 2011. Erratum: Experimental study on the air/water counter-current flow limitation in a model of the hot leg of a pressurized water reactor (Nuclear Engineering and Design). *Nuclear Engineering and Design*, *241*(8), 3359–3372. https://doi.org/10.1016/j.nucengdes.2011.02.028.

Deendarlianto, Höhne, T., Lucas, D., Vierow, K., 2012. Gas-liquid two-phase flow in a PWR hot leg: A comprehensive research review. *Nuclear Engineering and Design*, *243* (2), 214–233. https://doi.org/10.1016/j.nucengdes.2011.11.015.

Deendarlianto, D., Höhne, T., Lucas, D., Vallée, C., Zabala, G.A.M., 2011a. CFD studies on the phenomena around counter-current flow limitations of gas/liquid two-phase flow in a model of a PWR hot leg. Nuclear Engineering and Design 241 (12), 5138–5148. https://doi.org/10.1016/j.nucengdes.2011.08.071.

Deendarlianto, Höhne, T., Apanasevich, P., Lucas, D., Vallée, C., Beyer, M., 2012a. Application of a new drag coefficient model at CFD-simulations on free surface flows relevant for the nuclear reactor safety analysis. Annals of Nuclear Energy 39 (1), 70–82.

Deendarlianto, Ousaka, A., Kariyasaki, A., Fukano, T., 2005. Investigation of liquid film behavior at the onset of flooding during adiabatic counter-current air-water two-

phase flow in an inclined pipe. Nuclear Engineering and Design 235 (21), 2281–2294.
Deendarlianto, Ousaka, A., Indarto, Kariyasaki, A., Lucas, D., Vierow, K., Vallee, C., Hogan, K., 2010. The effects of surface tension on flooding in counter-current two-phase flow in an inclined tube. Experimental Thermal and Fluid Science 34 (7), 813–826.
do Amaral, C.E.F., Alves, R.F., da Silva, M.J., Arruda, L.V.R., Dorini, L., Morales, R.E.M., Pipa, D.R., 2013. Image processing techniques for high-speed videometry in horizontal two-phase slug flows. Flow Measurement and Instrumentation 33, 257–264.
dos Reis, E., Goldstein, L.J., 2010. Characterization of slug flows in horizontal piping by signal analysis from a capacitive probe. Flow Measurement and Instrumentation 21 (3), 347–355. https://doi.org/10.1016/j.flowmeasinst.2010.04.006.
Elperin, T., Klochko, M., 2002. Flow regime identification in a two-phase flow using wavelet transform. Experiments in Fluids 32 (6), 674–682. https://doi.org/10.1007/s00348-002-0415-x.
Gargallo, M., Schulenberg, T., Meyer, L., Laurien, E., 2005. Counter-current flow limitations during hot leg injection in pressurized water reactors. Nuclear Engineering and Design 235 (7), 785–804. https://doi.org/10.1016/j.nucengdes.2004.11.002.
Ghiaasiaan, S.M., Wu, X., Sadowski, D.L., Abdel-Khalik, S.I., 1997. Hydrodynamic characteristics of counter-current two-phase flow in vertical and inclined channels: Effects of liquid properties. International Journal of Multiphase Flow 23 (6), 1063–1083. https://doi.org/10.1016/s0301-9322(97)00027-x.
Ghosh, S., Pratihar, D.K., Maiti, B., Das, P.K., 2012. Identification of flow regimes using conductivity probe signals and neural networks for counter-current gas-liquid two-phase flow. Chemical Engineering Science 84, 417–436. https://doi.org/10.1016/j.ces.2012.08.042.
Ghosh, S., Pratihar, D.K., Maiti, B., Das, P.K., 2013. Automatic classification of vertical counter-current two-phase flow by capturing hydrodynamic characteristics through objective descriptions. International Journal of Multiphase Flow 52, 102–120. https://doi.org/10.1016/j.ijmultiphaseflow.2012.12.007.
Hudaya, A.Z., Widyatama, A., Dinaryanto, O., Juwana, W.E., Indarto, D., 2019. The liquid wave characteristics during the transportation of air-water stratified co-current two-phase flow in a horizontal pipe. Experimental Thermal and Fluid Science 103 (January), 304–317. https://doi.org/10.1016/j.expthermflusci.2019.01.021.
Jana, A.K., Das, G., Das, P.K., 2006. Flow regime identification of two-phase liquid-liquid upflow through vertical pipe. Chemical Engineering Science 61 (5), 1500–1515. https://doi.org/10.1016/j.ces.2005.09.001.
Jin, N.D., Nie, X.B., Ren, Y.Y., Liu, X.B., 2003. Characterization of oil/water two-phase flow patterns based on nonlinear time series analysis. Flow Measurement and Instrumentation 14 (4–5), 169–175. https://doi.org/10.1016/S0955-5986(03)00022-0.
Johnsson, F., Zijerveld, R.C., Schouten, J.C., Van Den Bleek, C.M., Leckner, B., 2000. Characterization of fluidization regimes by time-series analysis of pressure fluctuations. International Journal of Multiphase Flow 26 (4), 663–715. https://doi.org/10.1016/S0301-9322(99)00028-2.
Kinoshita, I., Nriai, T., Tomiyama, A., Lucas, D., Murase, M., 2011. Effects of Liquid Properties on CCFL in a Scaled-Down Model of a PWR Hot Leg. Journal of Power and Energy Systems 5 (3), 316–329. https://doi.org/10.1299/jpes.5.316.
Lucas, D., Rzehak, R., Krepper, E., Ziegenhein, T., Liao, Y., Kriebitzsch, S., Apanasevich, P., 2016. A strategy for the qualification of multi-fluid approaches for nuclear reactor safety. Nuclear Engineering and Design 299, 2–11. https://doi.org/10.1016/j.nucengdes.2015.07.007.
Lucas, D., Beyer, M., Pietruske, H., Szalinski, L., 2017. Counter-current flow limitation for air-water and steam-water flows in a PWR hot leg geometry. Nuclear Engineering and Design 323 (April), 56–67. https://doi.org/10.1016/j.nucengdes.2017.07.032.
Ma, Y., Shao, J., Lyu, J., Peng, J., 2020. Experimental study on the effect of diameter on gas–liquid CCFL characteristics of horizontal circular pipes. Nuclear Engineering and Design 364 (516), 110645. https://doi.org/10.1016/j.nucengdes.2020.110645.
Mayinger, F., Weiss, P., Wolfert, K., 1993. Two-phase flow phenomena in full-scale reactor geometry. Nuclear Engineering and Design 145 (1–2), 47–61. https://doi.org/10.1016/0029-5493(93)90058-H.
Minami, N., Nishiwaki, D., Nariai, T., Tomiyama, A., Murase, M., 2010. Countercurrent gas-liquid flow in a pwr hot leg under reflux cooling (i) air-water tests for 1/15-scale model of a pwr hot leg. Journal of Nuclear Science and Technology 47 (2), 142–148. https://doi.org/10.1080/18811248.2010.9711938.
Montoya, G.A., Deendarlianto, Lucas, D., Höhne, T., Vallée, C., 2012. Image-processing-based study of the interfacial behavior of the countercurrent gas-liquid two-phase flow in a hot leg of a PWR. Science and Technology of Nuclear Installations 2012, 1–10.
Morshed, M., Khan, M.S., Rahman, M.A., Imtiaz, S., 2020. Flow regime, slug frequency and wavelet analysis of air/Newtonian and air/non-Newtonian two-phase flow. Applied Sciences (Switzerland) 10 (9). https://doi.org/10.3390/app10093272.
Navarro, M.A., 2005. Study of countercurrent flow limitation in a horizontal pipe connected to an inclined one. Nuclear Engineering and Design 235 (10–12), 1139–1148. https://doi.org/10.1016/j.nucengdes.2005.02.010.
Nguyen, V.T., Euh, D.J., Song, C.H., 2010. An application of the wavelet analysis technique for the objective discrimination of two-phase flow patterns. International Journal of Multiphase Flow 36 (9), 755–768. https://doi.org/10.1016/j.ijmultiphaseflow.2010.04.007.
Ohnuki, A., 1986. Experimental study of counter-current two-phase flow in horizontal tube connected to inclined riser. Journal of Nuclear Science and Technology 23 (3), 219–232. https://doi.org/10.1080/18811248.1986.9734975.
Ousaka, A., Deendarlianto, K., A., Fukano, T., 2006. Prediction of flooding gas velocity in gas-liquid counter-current two-phase flow in inclined pipes. Nuclear Engineering and Design 236 (12), 1282–1292. https://doi.org/10.1016/j.nucengdes.2005.12.001.
Petritsch, G., Mewes, D., 1999. Experimental investigations of the flow patterns in the hot leg of a pressurized water reactor. Nuclear Engineering and Design 188 (1), 75–84. https://doi.org/10.1016/S0029-5493(99)00005-9.
Prayitno, S., Santoso, R.A., Deendarlianto, Höhne, T., Lucas, D., 2012. Counter current flow limitation of gas-liquid two-phase flow in nearly horizontal pipe. Science and Technology of Nuclear Installations 2012, 1–9.
Rodrigues, R.L.P., Cozin, C., Naidek, B.P., Marcelino Neto, M.A., da Silva, M.J., Morales, R.E.M., 2020. Statistical features of the flow evolution in horizontal liquid-gas slug flow. Experimental Thermal and Fluid Science 119 (May). https://doi.org/10.1016/j.expthermflusci.2020.110203.
Samal, K., Ghosh, S., 2020. Characterization and prediction of flow-conditions in the hot-leg of PWR during loss of coolant accident. Nuclear Engineering and Design 359 (December 2019), 110446. https://doi.org/10.1016/j.nucengdes.2019.110446.
Setyawan, A., Indarto, D., 2016. The effect of the fluid properties on the wave velocity and wave frequency of gas-liquid annular two-phase flow in a horizontal pipe. Experimental Thermal and Fluid Science 71, 25–41. https://doi.org/10.1016/j.expthermflusci.2015.10.008.
Utanohara, Y., Kinoshita, I., Murase, M., Lucas, D., Vallée, C., Tomiyama, A., 2012. Numerical simulations for steam-water CCFL tests using the 1/3 scale rectangular channel simulating a PWR hot leg. Nuclear Engineering and Design 249, 14–23. https://doi.org/10.1016/j.nucengdes.2011.05.041.
Vallée, C., Nariai, T., Futatsugi, T., Tomiyama, A., Lucas, D., Murase, M., 2012a. Experimental characterisation of the interfacial structure during counter-current flow limitation in a model of the hot leg of a PWR. Science and Technology of Nuclear Installations 2012, 1–8.
Vallée, C., Seidel, T., Lucas, D., Beyer, M., Prasser, H.M., Pietruske, H., Schütz, P., Carl, H., 2012b. Counter-current flow limitation in a model of the hot leg of a PWR - Comparison between air/water and steam/water experiments. Nuclear Engineering and Design 245, 113–124. https://doi.org/10.1016/j.nucengdes.2012.01.001.
Widyatama, A., Dinaryanto, O., Indarto, D., 2018. The development of image processing technique to study the interfacial behavior of air-water slug two-phase flow in horizontal pipes. Flow Measurement and Instrumentation 59 (2018), 168–180. https://doi.org/10.1016/j.flowmeasinst.2017.12.015.
Wijayanta, S., Indarto, D., Catrawedarma, I.G.N.B., Hudaya, A.Z., 2022. Statistical characterization of the interfacial behavior of the sub-regimes in gas-liquid stratified two-phase flow in a horizontal pipe. Flow Measurement and Instrumentation 83 (2), 102107. https://doi.org/10.1016/j.flowmeasinst.2021.102107.
Wijayanta, S., Indarto, D., Prasetyo, A., Hudaya, A.Z., 2023. International Journal of Multiphase Flow The effect of the liquid physical properties on the wave frequency and wave velocity of co-current gas-liquid stratified two-phase flow in a horizontal pipe. International Journal of Multiphase Flow 158 (2), 104300. https://doi.org/10.1016/j.ijmultiphaseflow.2022.104300.
Wongwises, S., 1994. Experimental Investigation of Two-Phase Countercurrent Flow Limitation in a Bend between Horizontal and Inclined Pipes. Experimental Thermal and Fluid Science 8 (3), 245–259.
Wongwises, S., 1996. Two-phase countercurrent flow in a model of a pressurized water reactor hot leg. Nuclear Engineering and Design 166, 121–133. https://doi.org/10.1016/j.nucengdes.2010.08.016.
Zapke, A., Kröger, D.G., 1996. The influence of fluid properties and inlet geometry on flooding in vertical and inclined tubes. International Journal of Multiphase Flow 22 (3), 461–472. https://doi.org/10.1016/0301-9322(95)00076-3.
Zhang, W.H., Li, H., Li, X., 2010. Identification of regime transitions in an inner-loop airlift reactor using local bubble-induced pressure fluctuation signals. Chemical Engineering Journal 162 (1), 296–300. https://doi.org/10.1016/j.cej.2010.04.038.